

Journal Pre-proofs

Plasticization -assisted slow crack growth modeling of high-density polyethylene

Abdulla Almomani, Jung-Wook Wee, Suleyman Deveci, Abdel-Hamid I. Mourad

PII: S0013-7944(24)00510-1
DOI: <https://doi.org/10.1016/j.engfracmech.2024.110347>
Reference: EFM 110347

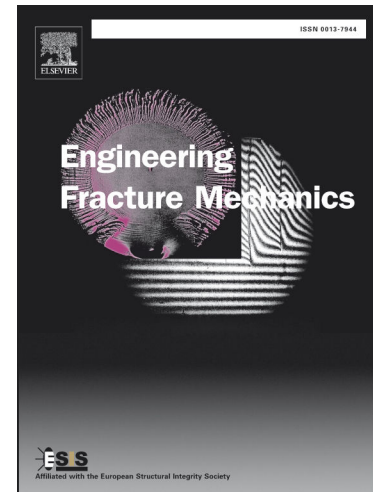
To appear in: *Engineering Fracture Mechanics*

Received Date: 3 June 2024
Revised Date: 22 July 2024
Accepted Date: 26 July 2024

Please cite this article as: Almomani, A., Wee, J-W., Deveci, S., Mourad, A.I., Plasticization -assisted slow crack growth modeling of high-density polyethylene, *Engineering Fracture Mechanics* (2024), doi: <https://doi.org/10.1016/j.engfracmech.2024.110347>

This is a PDF file of an article that has undergone enhancements after acceptance, such as the addition of a cover page and metadata, and formatting for readability, but it is not yet the definitive version of record. This version will undergo additional copyediting, typesetting and review before it is published in its final form, but we are providing this version to give early visibility of the article. Please note that, during the production process, errors may be discovered which could affect the content, and all legal disclaimers that apply to the journal pertain.

© 2024 Elsevier Ltd. All rights are reserved, including those for text and data mining, AI training, and similar technologies.



Plasticization-assisted slow crack growth modeling of high-density polyethylene

Abdulla Almomani^{1,3}, Jung-Wook Wee⁴, Suleyman Devenci³, and Abdel-Hamid I. Mourad^{1,2,*}

¹ Department of Mechanical and Aerospace Engineering, College of Engineering, United Arab Emirates University, Al-Ain, P.O. Box 15551, United Arab Emirates

² National Water and Energy Center, United Arab Emirates University, Al Ain, P.O. Box 15551, United Arab Emirates

³ Borouge Pte. Ltd, PO 6951, Abu Dhabi, United Arab Emirates

⁴ School of Mechanical System Engineering, Kumoh National Institute of Technology, Gumi, Gyeongbuk, 39177, Republic of Korea

*Corresponding Authors Emails: ahmourad@uaeu.ac.ae

Abstract

The existing crack layer model can theoretically predict the slow crack growth behavior of high-density polyethylene. However, it can only be applied to oxidative environments causing chemical degradation. Most oil and gas field components, such as pressurized pipes, are subjected to hydrocarbon exposures, leading to a plasticized material response, i.e., shear yielding instead of crazing. Therefore, the effect of such sorptive media diffusion on the slow crack growth behavior and lifespans t_f should be understood. In this work and for the first time, a novel crack layer model is developed that can simulate the diffusion-assisted slow crack growth behavior of plasticized high-density polyethylene. The proposed model was validated by comparing its prediction with experimental results and by conducting a sensitivity study on several input parameters. Using the proposed model, the reported plasticization results were reconstructed successfully including the SCG rate with $R^2 = 0.95$. This study expands the applicability of the crack layer model for the reliability assessment of polyethylene pipes under various environmental conditions, including plasticizers.

Keywords: Crack layer theory; Slow crack growth; High density polyethylene; Diffusion; Plasticization; Lifetime prediction.

Acronyms

AZ	Active zone
BBT	Bell telephone tests
CF	Configurational force
CL	Crack layer
CRB	Cracked round bar
COD	Crack opening displacement
DB	Dugdale–Barenblatt
ERR	Energy release rate
FEA	Finite element analysis
FNCT	Full-notch creep tests
HDPE	High density polyethylene
LEFM	Linear elastic fracture mechanics
LHC	Liquid hydrocarbons
NCTL	Notched constant tensile load
SCG	Slow crack growth
SIF	Stress intensity factor
SFE	Specific fracture energy
SSY	Small-scale yielding
TIP	Thermodynamics of irreversible processes
PZ	Process zone
WZ	Wake zone
WCTSE	Weight function complex Taylor series expansion

List of Symbols

K	Stress Intensity Factor
K_{Ic}	Mode I critical stress intensity factor
k_{CR}, k_{PZ}	Crack and process zone kinetic coefficients

L	Crack length and process zone length
L	Crack layer length
G_{tot}	Total Gibbs potential energy
G^{SIF}, G^{COD}	Green function for stress intensity factor and crack opening displacement
t_f	Time to failure
σ_{dr}	Drawing stress
σ_b	Boundary traction stress
δ_{tot}	Crack opening displacement
λ	Natural drawing ratio
a	Crack length of elastic body
A, m, n	Material parameters
W	Crack line width
X^{CR}, X^{PZ}	Crack and process zone corresponding driving forces
l^{CR}	Length of the Crack
J_1^{CR}, J_1^{PZ}	The Energy release rate for the crack and process zone
R_I	Volumetric quantity of transformed material to PZ
E'	The elastic modulus
2γ	Specific fracture energy
$2\gamma_0$	Initial specific fracture energy of fresh material
γ^{tr}	Transformation energy per unit volume
β_n	Coefficients for Green's function for stress intensity factor
μ_i	Coefficients for correction factor

High-density polyethylene (HDPE) pipes are widely used in key industrial applications such as nuclear and oil and gas networks [1-4]. This mandates an appropriate lifetime assessment given the material viscoelastic-viscoplastic behavior, and unique crack and plastic zone interplay [5-10]. In practical oilfield applications, the HDPE pipes can be exposed to a variety of liquid hydrocarbons. Hydrocarbons occur naturally and constitute the foundational elements of crude oil, natural gas, coal, and various other essential energy resources. Such hydrocarbons, with their non-polar aromatic and aliphatic molecular structure, can diffuse into the material by sorption affecting the material's yield and slow crack growth (SCG) behavior via plasticization, i.e., drop in modulus and yield strength [11-14]. HDPE can primarily exhibit three modes of failures, depending on the stress, temperature, and media exposed, namely large-scale yielding (region I), SCG (region II), and large-scale molecular degradation (region III) [15-17]. However, the underlying micro-deformation mechanisms, within the process zone (PZ), can change in plasticized HDPE from crazing and fibril breakdown to shear yielding with continuum flow [7].

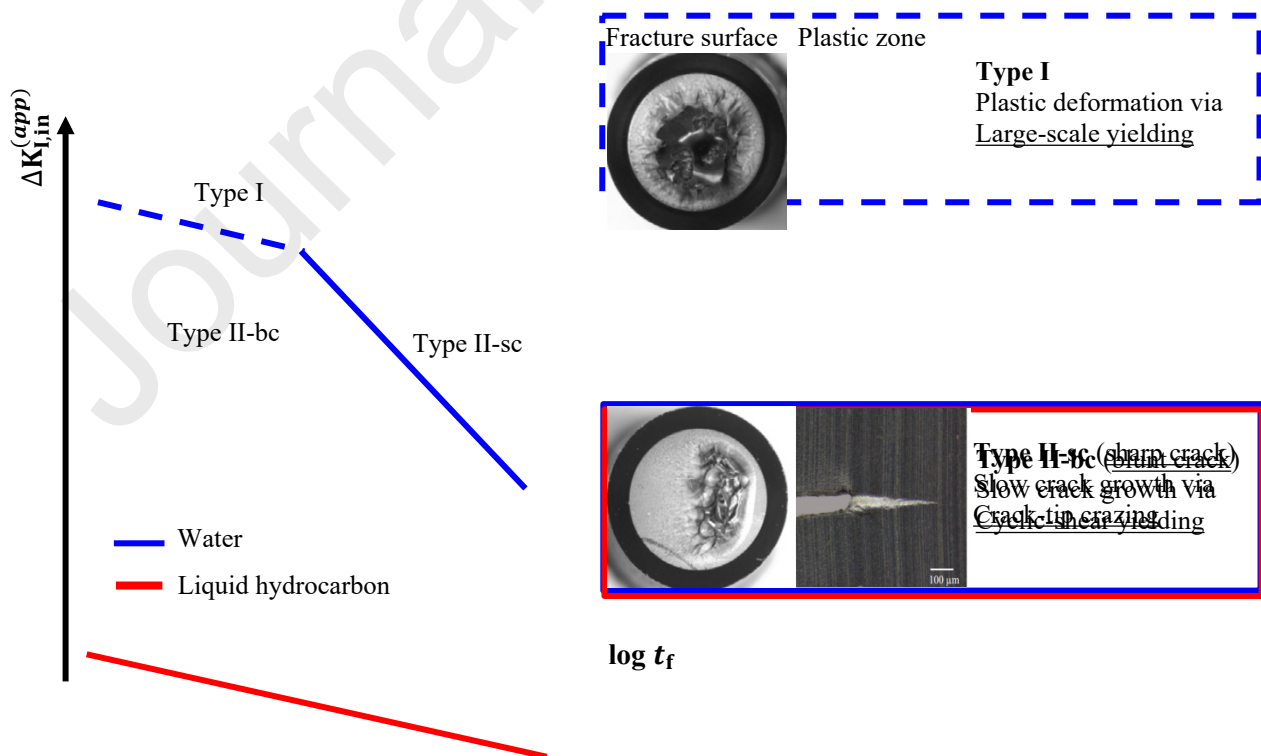
Schoeffl et al. [18] through tests on cracked round bar (CRB) specimens in 90/10 wt% i-octane/toluene revealed that shear yielding takes place at the crack-tip, unlike their propagation in water or air by fibril crazing. In addition, the physical crack-tip was found to appear significantly blunted. A voluminous irreversible deformation zone, due to hydrocarbons diffusion, can develop ahead of the crack tip driven primarily by shear band formation, unlike the wedge-like PZ in air, as shown in Fig. 1(a). The deformation mechanism in this region shifts from local crack-tip crazing to large-scale yielding that fails by cyclic yielding and advances via tearing. Schilling et al. [19, 20] through bell telephone tests (BTT) in diesel and biodiesel observed similar blunting and swelling effects during the crack initiation. In addition, full-notch creep tests (FNCT) showed further SCG acceleration, as outlined in Fig. 1(b), and more uniform roughness distribution induced by the enhanced chain mobility from such sorptive liquids. Wee et al. [21] through studying notched constant tensile load (NCTL) tests, also reported remarkable plasticization and lifetime differences in polypropylene induced from the contact with sorptive oils, i.e., diffused agents.

Multiple methods, since the 1950s, have been developed to estimate the lifetime of HDPE under gaseous hydrocarbon media. Yet, no protocol does exist presently that accounts for the SCG under liquid hydrocarbon environments [22]. Instead, such protocols do consider the exposure to gas condensate through a nominal reduction of mechanical strength [23, 24]. In light of the latter and given the changes in the PZ deformation mechanism in contact with plasticizers, as outlined in Fig. 2, capturing the physical aspect of fracture and the SCG process is fundamental for accurate lifetime predictions. SCG is a well reproducible process, unlike the poorly documented crack initiation which consequently facilitates lifetime modeling. Many of the empirical equations for SCG, e.g., Paris-Erdogan equation (power law), and the prevailing approaches are only applicable to a limited range of conditions and can't characterize more general crack growth scenarios [25]. Thuy et al. [26], for example, acknowledging such limitations used the Paris-Erdogan equation for modeling the plasticization induced SCG of HDPE in solvent-based liquids. This, nevertheless, remains limited to linear elastic fracture mechanics (LEFM) conditions under small-scale yielding (SSY) and fails to capture broader scenarios and the SCG process. Kamaludin et al. [27], proposed a method using the energy release G and crack growth rates under LEFM and SSY conditions for PE materials immersed in Igepal solution. Although the approach takes into account the blunting of the crack tip, the use of G is only relaxation-controlled, quantified by the modulus change, the physics of plasticization is not incorporated. Alavi et al. [28], suggested an extended finite element method (XFEM) nonlinear framework to model the SCG of PE materials, using the cohesive zone model (CZM) [29, 30]. Meanwhile, Wang et al. [31], considered a viscous crack growth through demonstrating the role of the cohesive strength in viscoelastic materials. Although the deformation potentials for the PZ and CZ are

boundaries. Overall, the properties of the cohesive elements are calibrated by actual experimental data, and in general it is difficult to transfer such properties to other geometries.

The crack layer (CL) theory proposed by Chudnovsky [33] offers an effective framework that can reproduce such complex SCG modes in HDPE, e.g., continuous and discontinuous, their transition and any environmental degradation, if present, such as oxidation or plasticization. In the CL theory, the crack and the PZ are treated as a coupled system [34]. This way, the physical interaction amongst the two can be captured. Using thermodynamics of irreversible processes (TIP) [35], the configurational forces responsible for the crack and PZ growth can be determined which accounts for the energy dissipation needed for the generation of micro-damages [36-38]. Consequently, the various SCG kinetics of HDPE can be reproduced using the CL theory including their transitions [39, 40]. The CL simulation not only provides the HDPE component lifetime or SCG rate, but also produces the complete crack and PZ damage growth process. This gives the theory another advantage for industrial settings over the conventional empirical models.

Despite the various applications present for the CL theory [34, 41], its deployment to a wider range of environmental conditions is still lacking. The existing CL model has only been applied to oxidative environments, e.g., chlorine-based disinfected water, based on changes in the molecular weight from chains scission [42]. In oilfield applications, the majority of the pressurized HDPE pipes suffer from the exposure to hydrocarbons which can act as a strong plasticizer, and consequently deteriorate the pipe durability. A diffusion-assisted SCG model based on the CL theory is hence needed for the lifetime prediction of plasticized HDPE in contact with such sorptive liquids. Therefore, the objective of this work is fourfold: (i) to develop a fundamental model using the CL theory for plasticized HDPE, (ii) to explain the associated physical mechanisms of plasticized HDPE within the PZ during the diffusion-assisted SCG process, (iii) to investigate the influence of temperature and plasticizer content on the lifetime variation of HDPE, and (iv) to compare the proposed model simulations with experimental diffusion-assisted SCG plasticized results from HDPE. Overall, this study aims to expand the applicability of the CL model for a reliable assessment of HDPE pipes' integrity and remaining life predictions in oilfields.



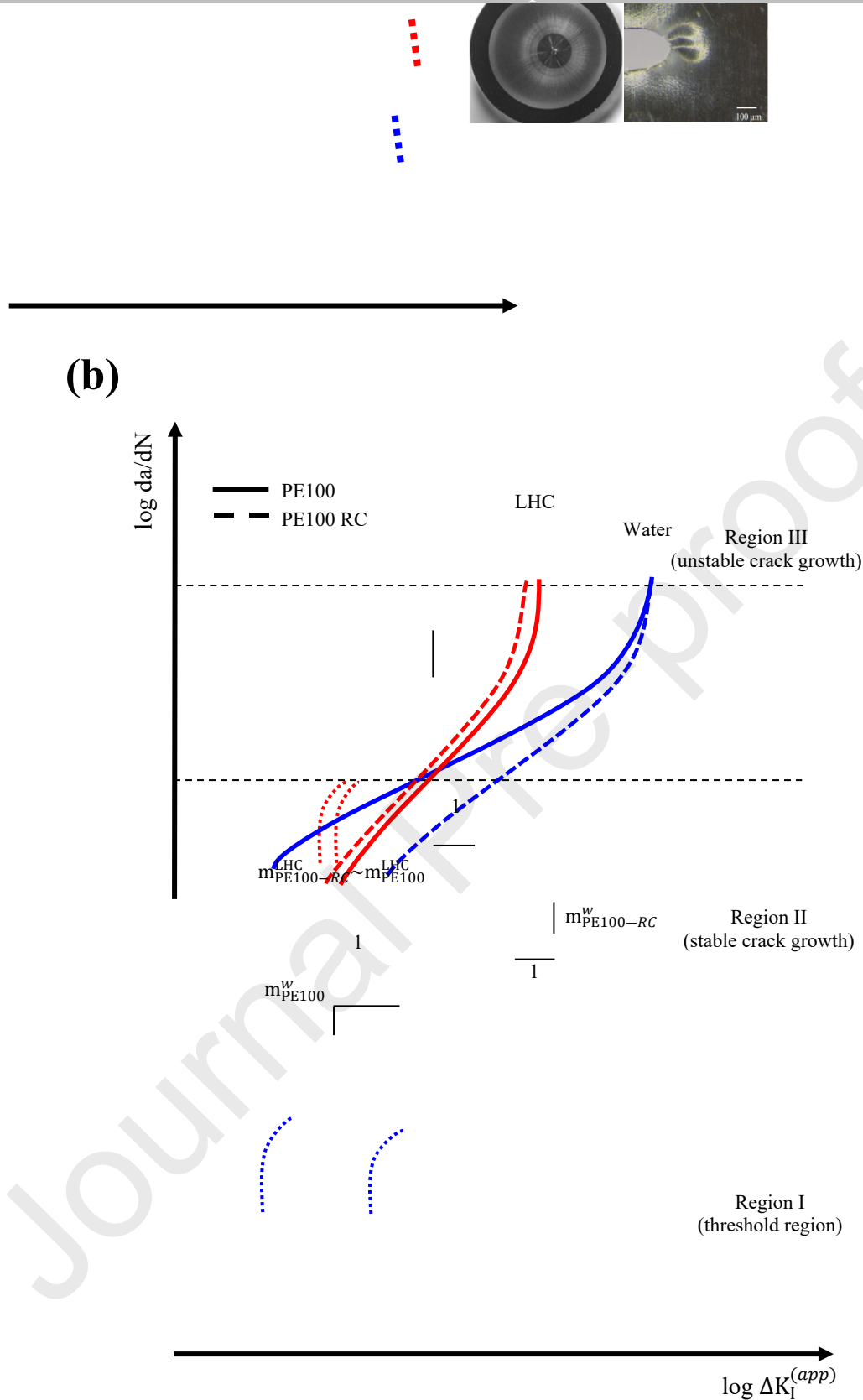


Fig. 1. An illustrative schematic comparing the behavior of HDPE in liquid hydrocarbons to water in a crack round bar (CRB) test, including the process zone (PZ) mechanism changes. (a) The PZ underlying deformation mechanism undergoes a transition from crack-tip crazing at a sharp crack to cyclic shear yielding within a blunt crack. This is also manifested by an acceleration of SCG failure time t_f . (b) A

2. Modification of the CL model to consider plasticization

The advances in materials science pose a significant challenge to the continuum damage mechanics (CDM) approach [43] in modeling the SCG process [44]. The main obstacle, obviously, lies within the hierarchy of interacting defects around the crack and adjacent PZ. One can neglect the microstructural details, for a thermodynamic treatment, which can be tackled through micromechanics [45-48]. The main objective of such treatment is to separately address the micromechanics for many of the equations parameters and derive a constative equation of the CL growth.

Despite many of the differences in morphology and molecular structure, under similar loading conditions, the observations for HDPE show that global evolution of microdefects array around the crack have several similar features. Overall, fracture including SCG are typically irreversible processes [49]. For that and in order to model the phenomenon, the framework of TIP can be employed. CL system would comprise of a crack and its adjacent damage. The CL propagation has been formulated on the basis of TIP including energy balance. It should be noted, however, that in the majority of structural applications, fatigue cracks of relevance are often small for a significant fraction of the structural life. The growth rates of such cracks with the standard procedures, e.g., ASTM E647 [50], are usually of little use in assessing the operational life of HDPE pipes. This emphasizes the need for large fracture mechanics geometries and in establishing a correlation between a specimen test data and the actual SCG behavior of an HDPE pipe geometry. Next, the thermodynamic considerations of the CL growth will be discussed.

2.1 Thermodynamic considerations of CL growth

To describe the CL growth thermodynamically, a list of state parameters needs to be introduced through introducing a damage parameter, following the energy equivalence principle that is recently used for polymers [51-54]. The entropy production [55] will need to be derived in order to deduce ‘thermodynamic causes’ of damage. This leads to the formulation of local energy balance, as follows:

$$\dot{u} = \tilde{\sigma} : \dot{\tilde{\epsilon}} - \tilde{\nabla} \cdot \tilde{j}^Q \quad (1)$$

where \dot{u} is the rate of internal energy density, $\tilde{\epsilon}$ is a strain rate tensor, the product $\tilde{\sigma} : \dot{\tilde{\epsilon}}$ represents the rate of work density, $\tilde{\nabla} \cdot \tilde{j}^Q$ gives the rate of internal energy density due to heat transfer, (\tilde{j}^Q stands for heat flux). The total strain tensor, considering small deformations, can be decomposed into perfectly elastic $\tilde{\epsilon}^{(e)}$ (thermodynamically reversible) and nonelastic $\tilde{\epsilon}^{(i)}$ (irreversible) parts, i.e.,

$$\tilde{\epsilon} = \tilde{\epsilon}^{(e)} + \tilde{\epsilon}^{(i)} \quad (2)$$

Part of the work done on nonelastic deformation is converted into heat. However, the other part is spent on damage nucleation and growth. The irreversible work related to damage growth and nucleation can be expressed as $\alpha \tilde{\sigma} : \dot{\tilde{\epsilon}}^{(i)}$, whereas $(1 - \alpha) \tilde{\sigma} : \dot{\tilde{\epsilon}}^{(i)}$ is converted into heat. Herein α is a phenomenological coefficient. Considering the left part of Eq. (1), the internal energy density u conventionally comprises of the entropic part Ts and Helmholtz free energy density f . This leads to \dot{u} being expressed as follow:

$$\dot{u} = \dot{f} + T\dot{s} + s\dot{T} \quad (3)$$

The time rate of the entropy density \dot{s} can be split into two terms: $\dot{s} = \dot{s}_e + \dot{s}_i$ following the basic \dot{s}_e stands for the entropy density rate related to the quasi-equilibrium exchanges with the surrounding by heat and other forms of energy. Hence, the equilibrium entropy rate \dot{s}_e can be introduced in the following form:

$$\dot{s}_e = -\tilde{\nabla} \cdot \frac{1}{T} \tilde{j}^Q + (1 - \alpha) \tilde{\sigma} : \dot{\tilde{\epsilon}}^{(i)} + \Delta S \cdot \dot{\rho} \quad (4)$$

where the first term is entropy rate driven by the entropy flux $\tilde{j}^s = \frac{1}{T} \tilde{j}^Q$, the second term reflects the rise of entropy from the irreversible work $\tilde{\sigma} : \dot{\tilde{\epsilon}}^{(i)}$ heat generation, and the third term represents the entropy changes rate induced by localized transformation of the thermodynamic state such as crazing, shear banding, etc. $\Delta S\{\tilde{\sigma}, T, O\}$ reflects the entropy difference between the undamaged and damaged material. Whereas $\dot{\rho}$ reflects the rate of damage density. The absolute temperature and the stress tensor constitute the conventional part from the list of parameters of state. Therefore, it is suitable to employ Gibbs free energy density g . Where g is the difference between Helmholtz free energy density f and the work done on elastic deformation density $\tilde{\sigma} : \dot{\tilde{\epsilon}}^{(e)}$. Consequently, this leads to the following expression:

$$\dot{g} = \dot{f} - \tilde{\sigma} : \dot{\tilde{\epsilon}}^{(e)} - \dot{\tilde{\sigma}} : \tilde{\epsilon}^{(e)} \rightarrow \dot{g} + \dot{\tilde{\sigma}} : \tilde{\epsilon}^{(e)} = \dot{f} - \dot{\tilde{\sigma}} : \tilde{\epsilon}^{(e)} \quad (5)$$

Substituting 2, 3 and 4 into 1 and solving the energy balance equation with respect to the energy production rate \dot{s}_i , and considering 5, the following can be deduced:

$$T\dot{s}_i = \alpha \tilde{\sigma} : \dot{\tilde{\epsilon}}^{(i)} - \dot{g} - \dot{\tilde{\sigma}} : \tilde{\epsilon}^{(e)} - s\dot{T} - \Delta S \cdot \dot{\rho} - \frac{1}{T} \tilde{j}^Q \tilde{\nabla} T \quad (6)$$

In the TIP that describe the effect of the mechanical stresses on the rate of chemical reactions as well as on the diffusion process, it all starts from the general expression of the entropy production rate as a bi-linear form of the thermodynamic fluxes and corresponding thermodynamic forces. The most important issue is the so-called cross effects. The fluxes are the rate of an irreversible strain, such as a creep strain or plasticity, as well as the vector of the diffusion, i.e., mass transfer with the corresponding force, which is the gradient of the concentration of the diffusing substance. It was the Onsager proposition that the thermodynamic forces affect the corresponding fluxes as well as all other fluxes. This allows us to specify the Onsager relations between the fluxes and forces. It would be possible to show how the stress within the PZ may lead to crazing and diffusion. Now, the generalized damage parameter P of the CL system can be introduced [56]. Eventually, the following expression for the entropy production would be obtained, by decomposing \dot{g} into elastic potential energy density Π and the Gibb's free energy densities of damaged and undamaged material Δg ,

$$T\dot{s}_i = \alpha \tilde{\sigma} : \dot{\tilde{\epsilon}}^{(i)} - \frac{\partial(h+\Pi)}{\partial P} \dot{P} - \frac{1}{T} \tilde{j}^Q \tilde{\nabla} T + \dot{\zeta} \cdot A_f + \tilde{j}^m \tilde{\nabla} C + \tilde{j}^m \tilde{\nabla} P + \tilde{j}^m \tilde{\nabla} C \quad (7)$$

where the fourth term $\dot{\zeta}$ stands for the chemical flux; A_f is the reciprocal thermodynamic force, i.e., the chemical affinity. Chemical flux $\dot{\zeta}$ plays an important role in the SCG phenomenon in a chemically aggressive environment, within a field of mechano-chemistry. The fifth, sixth and seventh terms play a role in filtration and diffusion processes where $\tilde{\nabla} C$ and $\tilde{\nabla} P$ represents concentration and pressure gradient (thermodynamic driving forces). Mass flux in filtration and diffusion is represented by \tilde{j}^m .

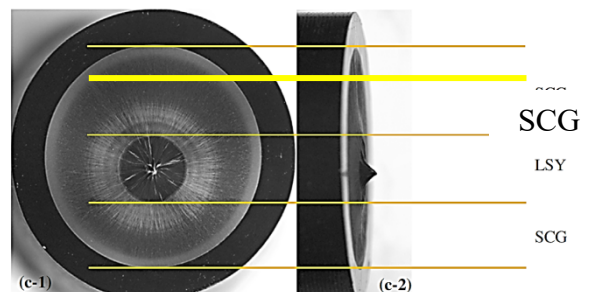
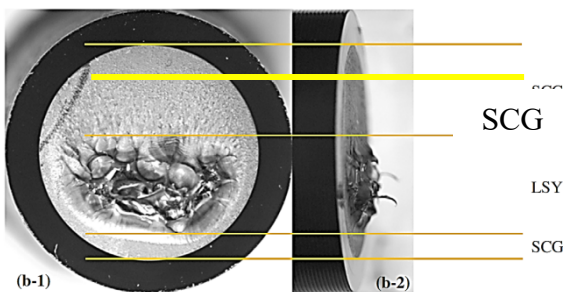
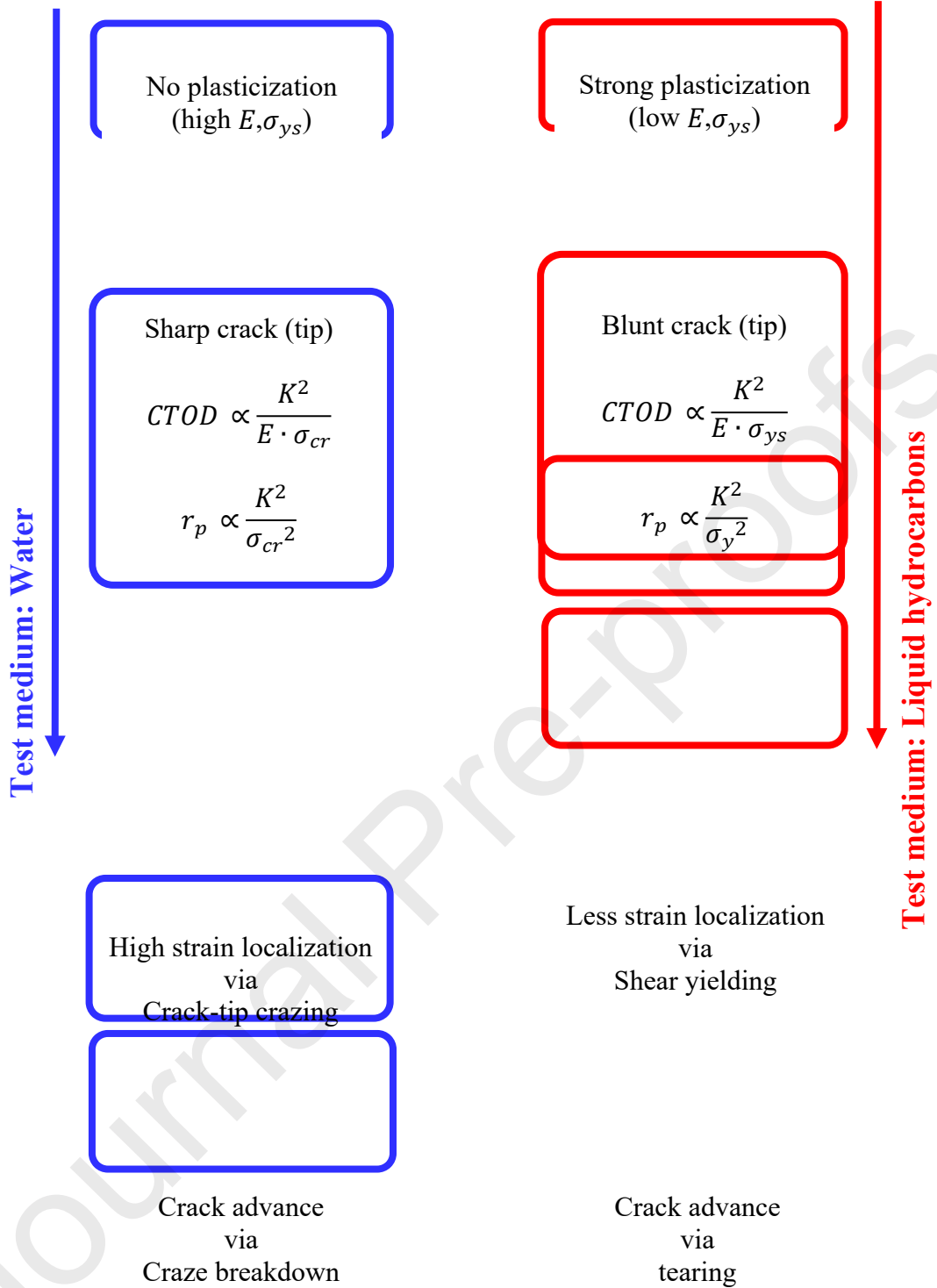




Fig. 2. (a) A schematic illustration of the chain of events PE 100 undergoes during the SCG in (a) water and (b) in liquid hydrocarbons under cyclic loading. Strong plasticization with a blunted crack tip can be observed in hydrocarbon medium. This leads to less strain localization via shear yielding and ultimately to a crack propagation through tearing [18].

For simplicity, a situation where both concentration and pressure gradients, $\tilde{\nabla}C$ and $\tilde{\nabla}P$, are zero for the time being can be assumed, i.e., considering a pre-saturated material state and a plasticized HDPE behavior. In order to concentrate attention on the damage process \dot{P} , we assume an isothermal condition and homogeneity of temperature field ($\tilde{\nabla}T = 0$). Under these conditions the entropy production Eq. (7) reduces to two terms, the first term is directly associated with damage and therefore is nonzero only within a region where $\dot{P} \neq 0$. The second term represents the entropy production due to damage growth \dot{P} directly. Then, the rate of global dissipation function $\dot{\Psi}$ with the irreversible damage evolution process under isothermal condition can be expressed as:

$$\dot{\Psi} = T\dot{S}_i = \dot{D} - \frac{\partial(\Pi + H)}{\partial P} \dot{P} \quad (8)$$

where the T is the temperature in kelvin, \dot{S}_i is the entropy production rate, and \dot{D} the rate of irreversible work related to damage growth and nucleation. Π and H reflects the present system potential energy and enthalpy, respectively.

2.2 Thermodynamic forces for CL growth in CRB specimen

An axisymmetric solid with a circumferential main crack, representing a CRB specimen, is considered here, which was constructed by Wee et al. in [38]. Fig. 3(a) and 3(b) illustrate the general CL configuration with a CRB specimen. The CL system consists of the main crack and the surrounding PZ. Within the PZ, two regions including the wake zone (WZ) and the active zone (AZ) can be divided. The time rate of continuous density $\dot{\rho}$ generated by shear yielding is zero in the WZ due to the traction-free nature on the crack face, and positive in the AZ. The CL configurational lengths are illustrated including the CL length L , the main crack length l_{CR} , and the CL width w . The AZ and the WZ are separated by a boundary called the trailing edge Γ_t , as outlined in Fig. 3(c). Meanwhile, the leading edge Γ_l reflects the AZ front edge, which represents the migration from the solid to the dotted boundary. $\delta\xi_i^{PZ}$ stands for the migration vector along Γ_l . The local coordinates in Fig. 3(c) are represented by the subscript i . The migration vectors on crack front edge Γ_{CR} , referred as $\delta\xi_i^{CR}$, is assumed to be directing into x_1 , and to be the same as δl_{CR} . Consequently, the rate of damage parameter \dot{P} in terms of the crack, PZ, and width configurational areas, A_{CR}, A_{PZ} and A_w , is expressed as follows [38]:

$$\dot{P} = \frac{\partial P}{\partial A_{CR}} \Big|_{A_w} \dot{A}_{CR} + \frac{\partial P}{\partial A_{PZ}} \Big|_{A_w} \dot{A}_{PZ} + \frac{\partial P}{\partial A_w} \Big|_{A_{CR}} \dot{A}_w \quad (9)$$

where $A_{CR} = \pi R^2 - \pi(R - l_{CR})^2$ and $A_w = \pi R^2 - \pi(R - l)^2$ reflects the crack face and CL area into Eq.(8) gives the following:

$$\dot{\Psi} = T\dot{S}_{irr} = \dot{D} + X^{CR}\dot{A}_{CR} + X^L\dot{A}_L + X^w\dot{A}_w \quad (10)$$

where X^χ , depending on the specific configurational parameter χ , stands for the relevant thermodynamic force (TF). For example, $X^{CR} = -\frac{\partial}{\partial A_{CR}}[\Pi + H]|_{A_L, A_w}$ reflects the TF for the expansion of A_{CR} , while A_L and A_w remain fixed. Physically, the thermodynamic fluxes are the time rate of configurational areas in Eq.(10). Linear irreversible thermodynamics can be used, assuming a quasi-equilibrium evolution of the CL. The thermodynamic fluxes can, therefore, be expressed as linear combinations of the TFs, as follows [57]:

$$\begin{bmatrix} \dot{A}_{CR} \\ \dot{A}_L \\ \dot{A}_w \end{bmatrix} = \begin{bmatrix} k_{11} & k_{12} & k_{13} \\ k_{21} & k_{22} & k_{23} \\ k_{31} & k_{32} & k_{33} \end{bmatrix} \begin{bmatrix} X^{CR} \\ X^L \\ X^w \end{bmatrix} \quad (11)$$

where k_{ij} reflects the kinetic coefficient tensor. Based on the Onsager's reciprocal theorem, k_{ij} is symmetric, meaning $k_{ij} = k_{ji}$. The corresponding fluxes is directly influenced by the diagonal elements in k_{ij} . Therefore, the TFs must be computed in advance in order to obtain the CL configurational fluxes, i.e., $\dot{A}_{CR}, \dot{A}_{PZ}$, and \dot{A}_w . For each corresponding flux, the TF, $X^\chi = -\frac{\partial}{\partial A_\chi}[\Pi + H]$, can be split into a driving term and resistance term, represented by $-\frac{\partial \Pi}{\partial A_\chi}$ and $-\frac{\partial H}{\partial A_\chi}$, respectively. The normalized vector components can be introduced for a better depiction of the PZ growth driving term [58]:

$$\begin{cases} \bar{\xi}_1^{PZ} = \frac{2\pi r_\xi \delta \xi_1^{PZ}}{2\pi(R_o - L)\delta L} \\ \bar{\xi}_2^{PZ} = \frac{2\pi r_\xi \delta \xi_2^{PZ}}{2\pi(R_o - l_{w,max})\frac{\delta w}{2}} \end{cases} \quad (12)$$

where r_ξ is the distance from the AZ boundary surface element to the center line, as outlined in Fig. 3(c). With that, the potential energy elemental release in relation to the CL configurational variation can be expressed as follows:

$$-\delta \Pi = \delta A_{CR} J_1^{CR} + \delta A_L J_1^{PZ} + \delta A_w J_2^{PZ} \quad (13)$$

where

$$\begin{cases} J_1^{CR} = \int_{\Gamma^{CR}} [P_{1j}^{PZ}] n_j dC \\ J_i^{PZ} = \int_{\Gamma_i} \bar{\xi}_i^{PZ} [P_{ij}^0 - P_{ij}^{PZ}] n_j dC \end{cases} \quad (14)$$

The potential energy Π can then be expressed as a function of configurational areas with $J_1^{CR} = -\frac{\partial \Pi}{\partial A_{CR}}$, $J_1^{PZ} = -\frac{\partial \Pi}{\partial A_L}$, and $J_2^{PZ} = -\frac{\partial \Pi}{\partial A_w}$. In Eq.(14), the P_{ij}^{PZ} and P_{ij}^0 represent the Eshelby tensor of the PZ and fresh materials, respectively [59].

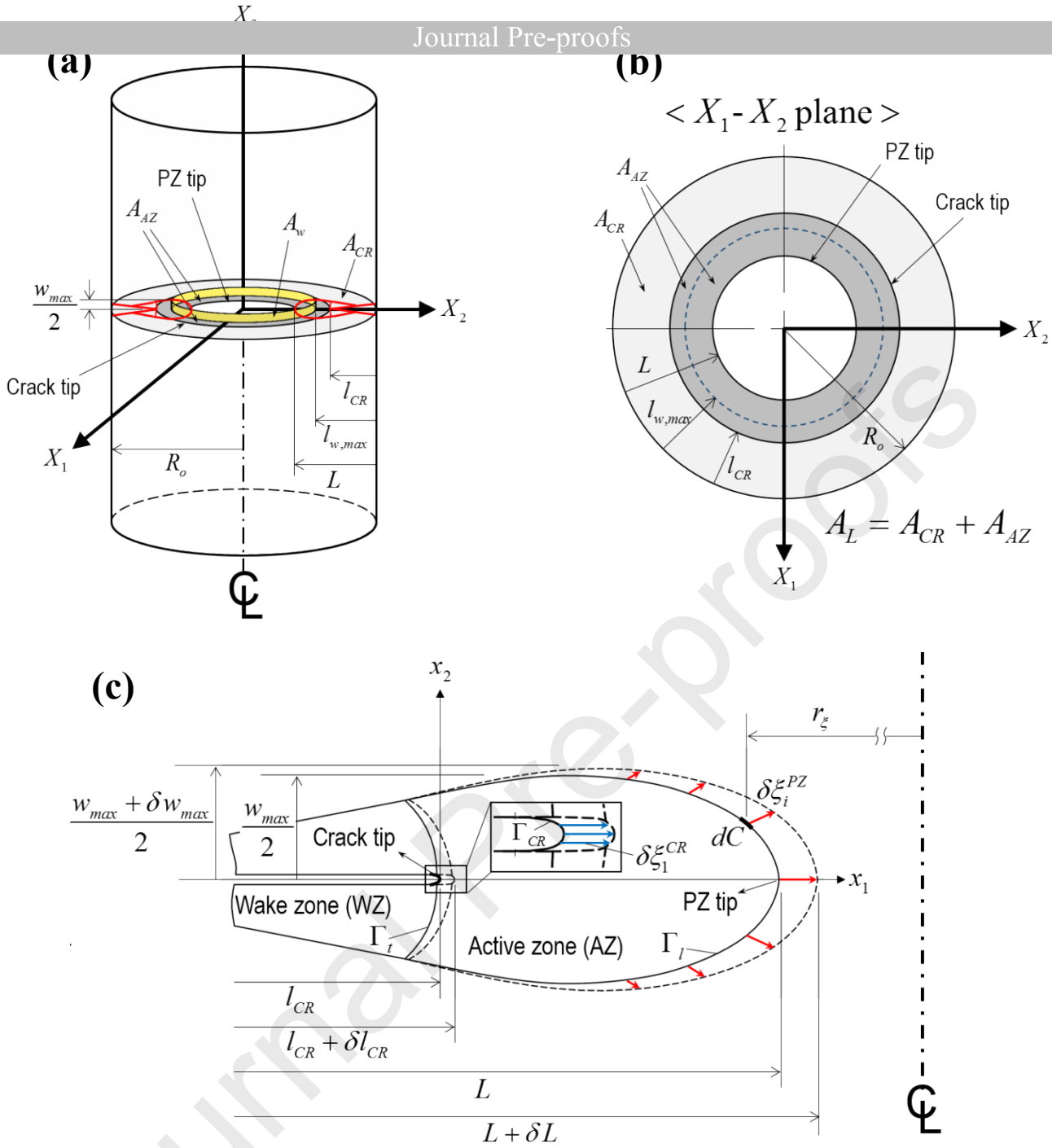


Fig. 3. A schematic illustration of an axisymmetric solid, representing a CRB specimen including the (a) CL configurational areas, e.g., the crack area A_{CR} , the AZ area A_{AZ} and the AZ width area A_w . The CL area A_L is the sum of the crack area A_{CR} and the AZ area A_{AZ} . (b) A top view of the CL configurational areas, in X_1 - X_2 plane. (c) An illustration of the circumferential CL configuration, highlighting the crack length l_{CR} , the CL length L , the PZ maximum width w_{max} and the migration vectors at the crack $\delta \xi_1^{CR}$ and AZ boundaries $\delta \xi_i^{PZ}$. The small elemental CL variations, e.g., δl_{CR} , δL , and δw , are also outlined [38].

The enthalpy of the CL system H is a volume integral of the enthalpy density $h = \gamma + \rho + h_0$, where γ_{sy} is the enthalpy jump due to shear yielding and per unit continuous area, whereas ρ reflects the continuous area induced by shear yielding per unit volume [56]. Herein, h_0 stands for the original enthalpy value of the undamaged material. Hence, the total enthalpy H variation driven by the CL evolution can be expressed as:

$$\delta H = 2\gamma \cdot \delta A_{CR} + \frac{\partial}{\partial A_L} \left[\int_{V_{AZ}} \gamma_{sy} \rho dV \right] \delta A_L + \frac{\partial}{\partial A_w} \left[\int_{V_{AZ}} \gamma_{sy} \rho dV \right] \delta A_w \quad (15)$$

where the 2γ is the specific fracture energy (SFE), i.e., the required enthalpy to generate a unit crack area. Whereas, V_{AZ} stands for the volume of the AZ. Setting the enthalpy jump per unit area γ_h as constant, the resistance terms become $\frac{\partial H}{\partial A_{CR}} = 2\gamma$, $\frac{\partial H}{\partial A_L} = \gamma_{sy} R_1^{PZ}$, and $\frac{\partial H}{\partial A_w} = \gamma_{sy} R_2^{PZ}$, where $R_1^{PZ} = \frac{\partial}{\partial A_L} \int_{V_{AZ}} \rho dV$ and $R_2^{PZ} = \frac{\partial}{\partial A_w} \int_{V_{AZ}} \rho dV$. In the CL theory, the undamaged elastic solid, the crack and the PZ are considered as separate phases. The principle of superposition is followed which uses the additive property of the SIF. The TFs for each phase growth are then derived from the variation in the system Gibbs free energy (∂G) with regard to the migration of each phase boundary. Hence, there would be three thermodynamic force (TF) equations for the CL system, one for the crack, another for the PZ growth, and one for the PZ width growth, i.e., X^{CR} , X^{PZ} , and X^w . The general expressions for the crack and PZ driving forces are formulated as [39]:

$$X^{CR} = -\frac{\partial G}{\partial A_{CR}}; X^{PZ} = -\frac{\partial G}{\partial A_L}; X^w = -\frac{\partial G}{\partial A_w} \quad (16)$$

Therefore, the TFs can be represented in the following simple forms:

$$\begin{cases} X^{CR} = J_1^{CR} - 2\gamma(\omega(x,t), t) \\ X^L = J_1^{PZ} - \gamma_{sy} R_1^{PZ} = \frac{K_{tot}^2}{E'} - \frac{\gamma^{tr}}{\epsilon_0} \delta_{tot} \\ X^w = J_2^{PZ} - \gamma_{sy} R_2^{PZ} \end{cases} \quad (17)$$

where J_1^{CR} is the energy release rate (ERR) due to one step crack growth into the PZ. Likewise, γ_{sy} stands for the specific energy of shear yielding that includes plastic deformation and the work of yielding, J_1^{PZ} is the ERR due to PZ unit advancement. Meanwhile, γ and γ_{sy} are the specific fracture energy of the PZ and the HDPE transformation energy for a single unit volume into yielded state. In addition, K_{tot} is the sum of the SIFs determined by superposition. Lastly, δ_{tot} is the crack opening displacement (COD) at the PZ-cutoff elastic solid crack tip. The non-zero value of the K_{tot} is what makes the difference between the CL and Dugdale-Barenblatt (DB) model equilibrium PZ which requires $K_{tot} = 0$.

driven primarily by shear band formation. This PZ shape can be simplified to represent a self-similar geometry ($l_{CR}, \dot{L} \gg w$) [58, 60]. With this, the CL configuration is primarily dominated by the crack length l_{CR} and the CL length L , as shown in Fig. 4, resulting in the CL having 2 degrees of freedom (D.O.F) configuration (\dot{l}_{CR} and \dot{L}). In addition, owing to the narrow shape assumed to the PZ, its boundary migration ERR in x_1 , direction, J_1^{PZ} , is approximated to be the same as PZ tip ERR. Furthermore, a clear boundary is set to separate the undamaged material from the PZ, consequently. These geometrical considerations will facilitate the deployment of the superposition principle, outlined in Fig. 4(c) through 5(f) [61]. The total CL shown in Fig. 4(c), under such conditions, can be separated into PZ-cutoff elastic material, shown in Fig. 4(d), and PZ medium, shown in Fig. 4(e). Since the plasticized PZ of HDPE comprises of yielded material, the traction over the separating boundary is assumed to be constant with the yield stress σ_y of the pre-saturated HDPE. The PZ tip ERR can be computed as illustrated in Fig. 4(d). The ERR can then be expressed as $J_1^{PZ} = (K_\infty + K_{dr})^2/E'$, assuming an elastic response to the PZ cut-off medium, where K_∞ and K_{dr} stand for the mode I stress intensity factor (SIF) due to the applied stress σ_∞ and yield stress σ_y , respectively. The E' stands for the plane strain elastic modulus.

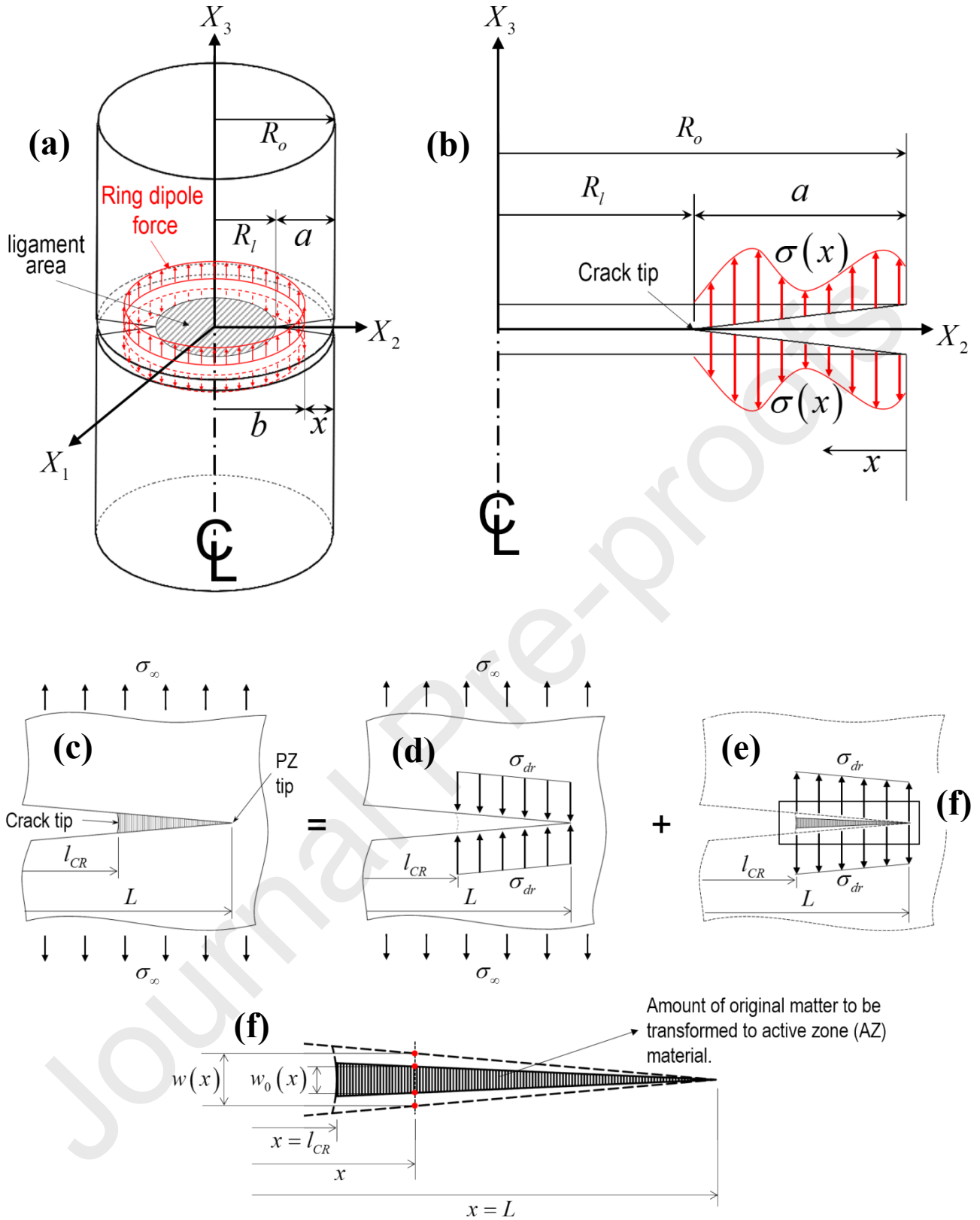


Fig. 4. (a) A CRB specimen subjected to a constant circumferential load i.e., a ring dipole force on the crack face, with a radius of $b = R_o - x$. The ligament radius is denoted R_l , while the crack length, measure from the outer surface, as a . (b) A schematic illustrating the crack face arbitrary loading in an axisymmetric way. The method of superposition to compute the total SIF at the PZ tip and COD within the AZ. The total CL (c) can be decomposed into PZ cutoff elastic material (d) and material to be transformed to AZ medium (e). The magnified view of PZ material is depicted in (f) [38].

2.3 Plasticization of the PZ material

The continuous density ρ inside the PZ of pre-saturated and plasticized HDPE can be assumed constant within the AZ. Therefore, ρ in the integral of R_1^{PZ} can come out. Thus, the R_1^{PZ} is given by $R_1^{PZ} = \gamma_{sy} \frac{\partial}{\partial A_L} \left[\int_{V_{AZ}} \rho dV \right] = \gamma^{tr} \frac{\partial V_{AZ}}{\partial A_L}$, where the $\gamma^{tr} = \gamma_{sy} \rho$ refers to the energy required for the shear yielding process within the AZ, per unit volume. The V_{AZ} refers to the transformed original HDPE volume into AZ, as shown in Fig. 4(f). By setting the original width of the material to be $w_0(x)$, and the current yielded width of the AZ as $w(x)$, the increase in width $\Delta w(x)$ can be computed. A superposition of the crack opening displacement (COD) due to remote stress σ_∞ , denoted $\delta_\infty(x)$, and the COD developed from the yield stress σ_y , denoted $\delta_{sy}(x)$, where x is a distance measured from the outer surface. Therefore, $\Delta w(x)$ can be written as $\Delta w(x) = \delta_{tot}(x) = \delta_\infty(x) + \delta_{sy}(x)$.

Without plasticization, the CL model assumes the resistance of the PZ material to crack extension decreases with time. The PZ material is said to degrade with time through crazing i.e., fibril creep and breakdown, as shown in Fig 5(a). In the plasticized state, the PZ formation occurs under the yield stress σ_y and with stretching subject to the strain at yield ε_0 , as outlined in Fig 5(b). The PZ is incompressible, so the true stress acting on the PZ is defined to be $(1 + \varepsilon_0)\sigma_y$. The surface energy 2γ represents a measure of the PZ resistance to crack extension. The PZ consists of voluminous plasticized zone undergone irreversible deformation with no fibrils structure. The damage mechanism in the PZ shifts from local crack tip crazing to large-scale yielding by shear deformation. Hence, the crack advances via tearing instead of ligaments rupture.

If the PZ is deformed at time $t = 0$, it has an initial axial strain ε_0 . As time t increases, and the PZ continues to be subjected to a stress of $(1 + \varepsilon_0)\sigma_y$, the PZ axial strain ε will increase until the critical axial strain ε_c is reached, as outlined in Fig. 5(c). The sorption induced plasticization is represented by a drop in modulus E and yield stress σ_y . Thereafter, the PZ tears. The crack advances whenever the PZ at the crack tip tears. The width of the original material strip which is transformed into the PZ is $w(x)$. The crack layer opening displacement (CLOD) is defined as $\delta_{tot}(x) \equiv \varepsilon(x)w(x)$. From the strain definition $w(x) \equiv \frac{\delta_{tot}(x)}{\varepsilon_0}$. Considering a CRB specimen with outer radius of R_o , with the simple arrangements, the resistance term in the TF associated with the PZ growth can be expressed as:

$$\gamma_{sy} R_1^{PZ} = \gamma^{tr} \frac{\partial V_{AZ}}{\partial A_L} = \frac{\gamma^{tr}}{\varepsilon_0(R_o - L)} \cdot \frac{\partial}{\partial L} \left[\int_{l_{CR}}^L (R_o - x) \delta_{tot}(x) dx \right] \Big|_{l_{CR}=const.} \quad (18)$$

Consequently, the apparent TFs are:

$$\begin{cases} X^{CR} = J_1^{CR} - 2\gamma \\ X^L = \frac{K_{tot}^2}{E'} - \frac{\gamma^{tr}}{\varepsilon_0(R_o - L)} \cdot \frac{\partial}{\partial L} \left[\int_{l_{CR}}^L (R_o - x) \delta_{tot}(x) dx \right] \Big|_{l_{CR}=const.} \end{cases} \quad (19)$$

(a)

(b)

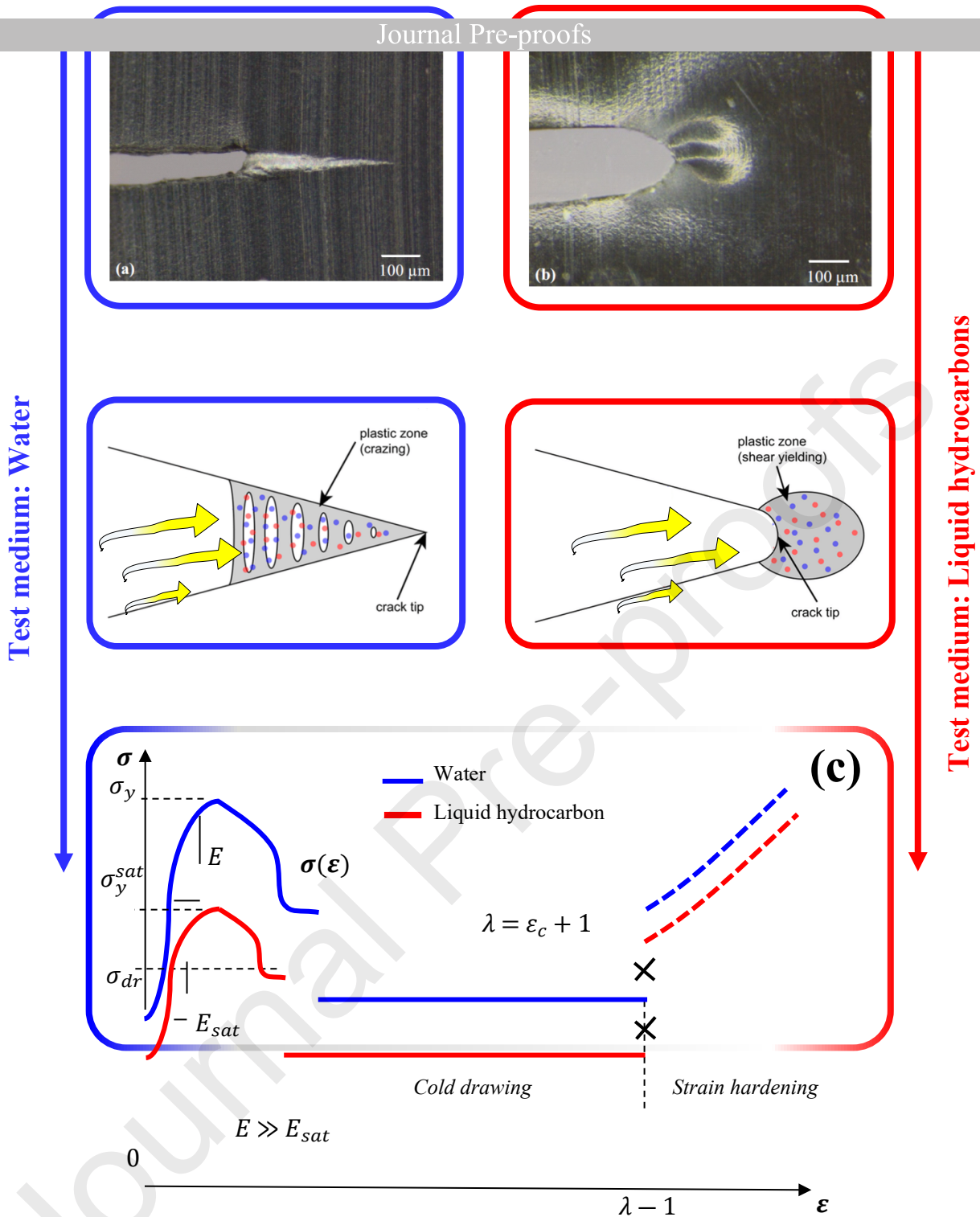


Fig. 5. A comparison of the PZ underlying deformation mechanisms between (a) water and (b) liquid hydrocarbons test mediums. The physical crack-tip in (b) liquid hydrocarbons appear significantly blunted [18]. A voluminous irreversible deformation zone, due to hydrocarbons diffusion, can develop ahead of the crack tip driven primarily by shear band formation, unlike the wedge-like PZ in (a) water or air. The deformation mechanism in this region shifts from local crack-tip crazing to large-scale yielding that fails by cyclic yielding and advances via tearing. (c) Representation of the stress-strain curves in water (blue) where HDPE undergoes drawing, unlike the softening and continuum flow in liquid hydrocarbons (red). The resultant softening is reflected by a shift of the yield stress σ_y to σ_y^{sat}

Journal Pre-proofs

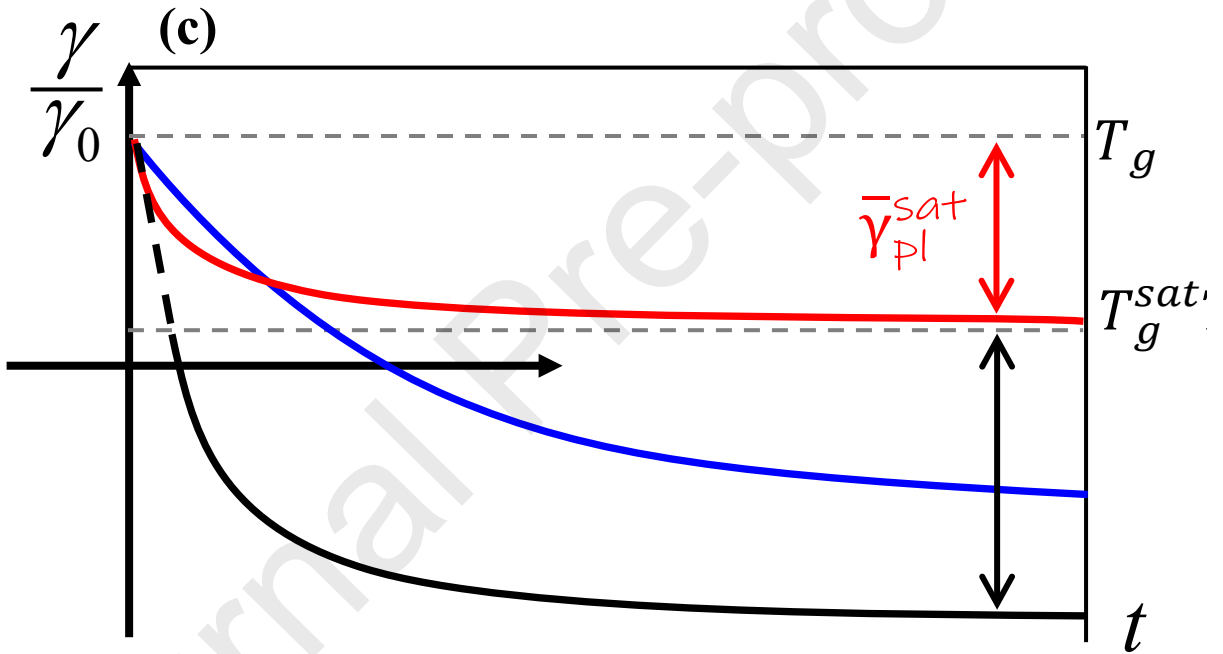
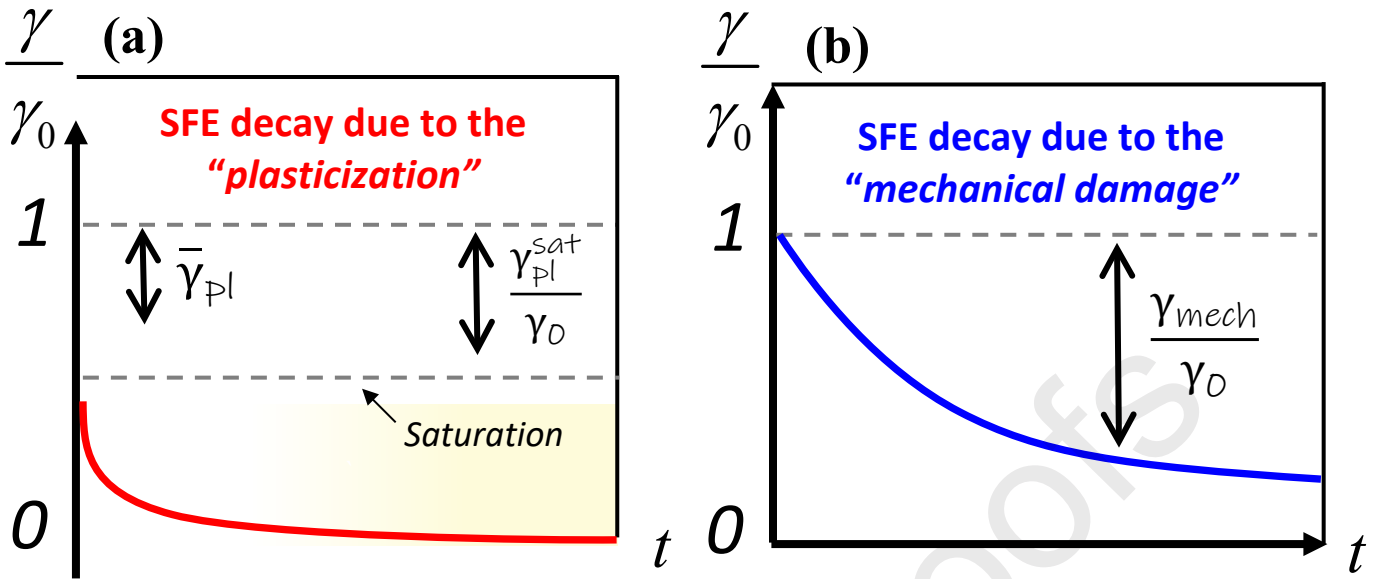
where the total SIF K_{tot} is the sum of the remote stress SIF K_{∞} and the yield stress SIF $K_{\infty} - K_{\infty} + K_{\infty}$. In order to simplify the way forward, only the direct influences between TFs and corresponding fluxes in Eq.(11) will be considered, neglecting any cross-effects. This leads to the simple relationships of $\dot{A}_{CR} = k_{CR}X^{CR}$ and $\dot{A}_L = k_L X^L$, where the $k_{11} = k_{CR}$ and $k_{22} = k_L$. Therefore, the rate of configurational lengths, \dot{l}_{CR} and \dot{l}_L , can be expressed as:

$$\begin{cases} \dot{l}_{CR} = \frac{k_{CR}X^{CR}}{2\pi(R_o - l_{CR})} \\ \dot{l}_L = \frac{k_L X^L}{2\pi(R_o - L)} \end{cases} \quad (20)$$

Eq.(20) hold true under the condition of a positive TF. If the TF is computed as a negative value, the rate of configurational lengths is zero since the irreversibility of the process is physically impossible. A small incremental crack and PZ lengths can be calculated, if Eq. (20) is multiplied by a small-time increment Δt . With that, by applying a time-marching loop to Eq. (19)-(20), the CL growth complete simulation can be achieved. 2γ in Eq.(19) is the SFE of the yielded material. SFE usually decays with time due to material's creep. This process is highly accelerated by the absorption and diffusion induced plasticization. Therefore, the SFE at each point x and time instance t is a function of $\omega(x,t)$ and a creep strain $\varepsilon^p(x,t)$. The SFE decays by the superposition of the sorption induced plasticization $\bar{\gamma}_{pl}^{sat}$, and the mechanical degradation $\bar{\gamma}_{mech}$, as outlined in Fig. 6, leading to the following expression:

$$\gamma_{tot}(\omega(x,t), \varepsilon^p(x,t)) = \gamma_{mech}(\varepsilon^p) + \gamma_{pl}(\omega(x,t)) = \gamma_{mech}(\varepsilon^p) + \gamma_0[(1 - \omega)^n - 1] \quad (21)$$

Quantitative modeling of the diffusion induced plasticization and the resulting deterioration of material resistance to fracture, i.e., SFE, one needs to introduce a degradation parameter, to monitor its evolution, and to establish relationship between the degradation parameter and material properties in question. The absorption of PE to a plasticizer, e.g., liquid hydrocarbons, can lead to a significant decrease in the glass transition temperature T_g , which consequently results in swelling and a shift of the maximum relaxation process β towards lower temperatures, as shown in Fig. 7 [62]. The theories about plasticization attempts to explain the mechanism of the phenomenon. In the lubricity theory [62], a plasticizer reduces the intermolecular friction between the polymer molecules. In the gel theory, it reduces the number of points of attachment of the polymer to polymer. Whereas, in the free volume theory [63], the plasticizer content is linked to the diminution of the glass transition temperature. The friction between molecules (or viscosity) is related to the volume between them, and so to the glass transition temperature, T_g . The free volume gradually increases with the rise of T_g up until a sufficient energy is met, wherein the chain enter a motion state [64].



$$\bar{\gamma}_{mech}$$

$$\bar{\gamma}_{tot}^{sat}$$



Fig. 6. A schematic of the specific fracture energy (SFE) decay by the superposition. (a) the sorption induced plasticization SFE $\bar{\gamma}_{pl}$ decaying until saturation is reached. (b) The mechanical degradation of the SFE $\bar{\gamma}_{mech}$ induced by material relaxation. (c) The superimposed total SFE decay $\bar{\gamma}_{tot}$ (solid black) comprised of the saturated SFE decay $\bar{\gamma}_{pl}^{sat}$ (solid red), as well as the mechanical SFE decay $\bar{\gamma}_{mech}$ (solid blue). The plasticized yet to be saturated SFE decay (dashed black) is also outlined. The impact of the drop in the glass transition temperature from T_g to the plasticized state T_g^{sat} upon saturation (dashed red) is manifested by a downward shift for $\bar{\gamma}_{tot}$ to $\bar{\gamma}_{tot}^{sat}$ by the height of $\bar{\gamma}_{pl}^{sat}$ (red arrows).

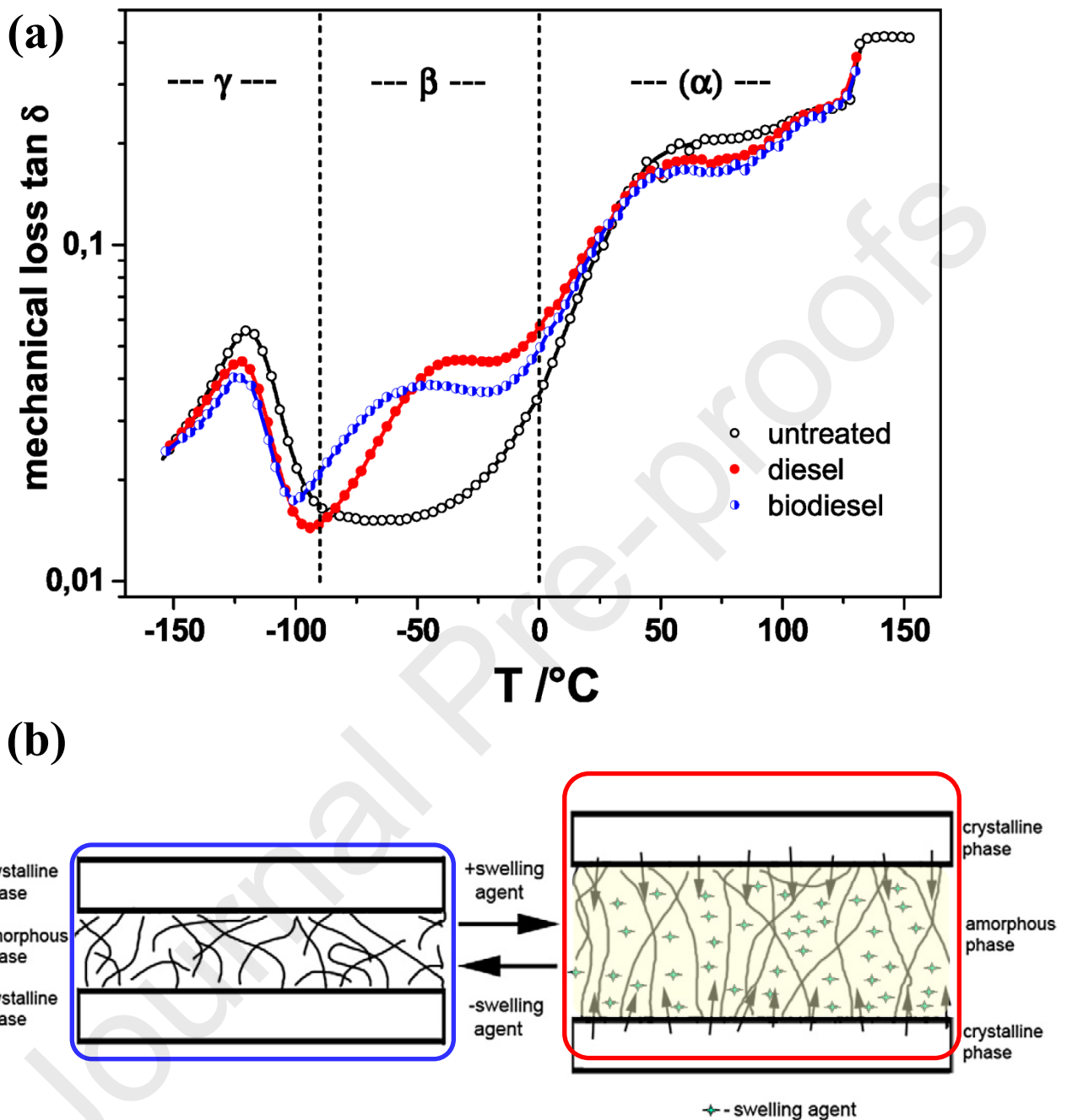


Fig. 7. An illustration of the clear correlation of the fuel sorption induced plasticization and drop in SFE with the enhanced β -relaxation observed by DMA. (a) Mechanical loss $\tan \delta$ of HDPE from torsion pendulum measurements after saturation in a plasticizer agent, e.g., diesel and biodiesel, compared to the untreated material [65]. (b) A schematic illustration of plasticization outlining the effect of sorptive liquids, e.g., hydrocarbons, microstructural changes in the amorphous phase induced by the sorption of the molecules of the plasticizer. This results in filling the free volumes within the amorphous phase and in size expansion, i.e., swelling [62].

Journal Pre-proofs

plasticizer concentration. Saad et al. [68], through studying the plasticizing effect of biodiesel on PE, reported observations of the necking regions after their immersion. The exposed samples exhibited a significant decrease in fibrillation. The absorbed biodiesel lubricated the inter-crystalline chains, similar to a stress-cracking agent, promoting crystal slippage during plastic deformation with no increase in internal stress. Overall, PE materials increase their mobility, i.e., properties of the matrix change, with increasing the concentration of a penetrant. This affects the rate of relaxation and the diffusion kinetics, which eventually control the rate of polymer displacement. In light of the above, a simple, easily measurable, and relevant degradation parameter $\omega(t)$ is naturally to express plasticization in terms of current and initial glass transition temperatures $T_g(t)$ and $T_g(0)$:

$$\omega(t) \equiv 1 - T_g(t)/T_g(0), \quad (22)$$

A number of experimental techniques have been developed to detect the plasticization effect of sorptive liquids by measuring the chains mobility, e.g., dynamic mechanical analysis (DMA), and to quantify extend of sorption by direct, e.g., gravimetric and mass balance, or indirect, e.g., differential scanning calorimetry (DSC), evaluation of T_g reduction. Finally, and in order to obtain K_{tot} and δ_{tot} (x) in Eq.(19), the Green's function (GF) of the SIF G_{CRB}^{SIF} and the COD G_{CRB}^{COD} , for the CRB specimen will be established and derived in the next section.

2.4.1 SIF Green's function

In order to construct the GF of an axisymmetric CRB specimen G_{CRB}^{SIF} , the SIF developed by a unit ring force applied on the crack upward and downward surfaces at a radius b is obtained. The geometry of the CRB specimen, including the crack l_{CR} , crack layer length L , the remote stress σ_∞ , and the drawing stress σ_{dr} is illustrated in Fig. 8(a). The SIF Green's function G_{inf}^{SIF} for a circumferential crack in infinite medium, with a ligament radius of R_l , and applied ring load at radius of b is given in Tada's handbook [69], as follows:

$$G_{inf}^{SIF} = \frac{2\pi b}{(\pi R_l)^{1.5}} \left\{ \cos^{-1} \left(\frac{R_l}{b} \right) + \frac{R_l}{\sqrt{b^2 - R_l^2}} \right\} \quad (23)$$

Therefore, the form of the G_{CRB}^{SIF} applicable to a CRB specimen can be arranged, as follows:

$$G_{CRB}^{SIF} = f(R_o, a, b) \cdot G_{inf}^{SIF} \quad (24)$$

where $f(R_o, a, b)$ represents the correction factor of the finite medium. This factor is typically larger than a unit value. The factors $\alpha = \frac{a-x}{a}$ and $\beta = \frac{R_o-a}{R_o}$ were used to normalize the geometries and force position b . $f(\alpha, \beta)$ is shown in Fig. 8(b) with a total of 63 data points ranging from $0 < \alpha < 1$ and $0.2 \leq \beta \leq 0.8$. Wee et al. [38] used a 4th order bivariate polynomial to fit $f(\alpha, \beta)$ comprising of 10 terms, and expressed as follows:

$$f(\alpha, \beta) = \alpha^3(C_1 + C_2\beta) + \alpha^2(C_3 + C_4\beta + C_5\beta^2) + \alpha\beta(C_6 + C_7\beta + C_8\beta^2) + C_9\beta + 1 \quad (25)$$

where the coefficients C_i are listed in Table 1. Fig. 8(b) shows the surface plot of Eq.(15) including the base data points indicated by white circles. It should be highlighted, as well, that when the normalized geometries and force position b approach zero, i.e., $\beta \rightarrow 0$ and $\alpha \rightarrow 0$, the correction factor $f \rightarrow 1$. This means that the GF approaches the circumferential crack in infinite medium analytical solution. Therefore, the Green's function obtained for SIF has a proper asymptotic response. With that, any load case of the CRB specimen SIF can be found by integrating $G_{CRB}^{SIF}(a, R_o; x) = f(\alpha, \beta) \cdot G_{inf}^{SIF(a, R_o; x)}$. For instance, the SIF at the crack tip for a CRB specimen with axisymmetric traction on the crack face is as follows:

$$K_I(a, R_o; \sigma(x)) = \int_0^a \sigma(x) \cdot G_{CRB}^{SIF}(a, R_o; x) dx \quad (26)$$

where the $\sigma(x)$ is an arbitrary traction on the crack face within $0 \leq x \leq a$, as shown in Fig. 4(b). The SIFs computed from Tada's handbook and the integration of $G_{CRB}^{SIF}(a, R_o; x)$ in Eq.(26) are plotted in Fig. 8(c), for comparison. The two SIFs agree markedly well for a reasonable range of crack length.

(a)

(c)

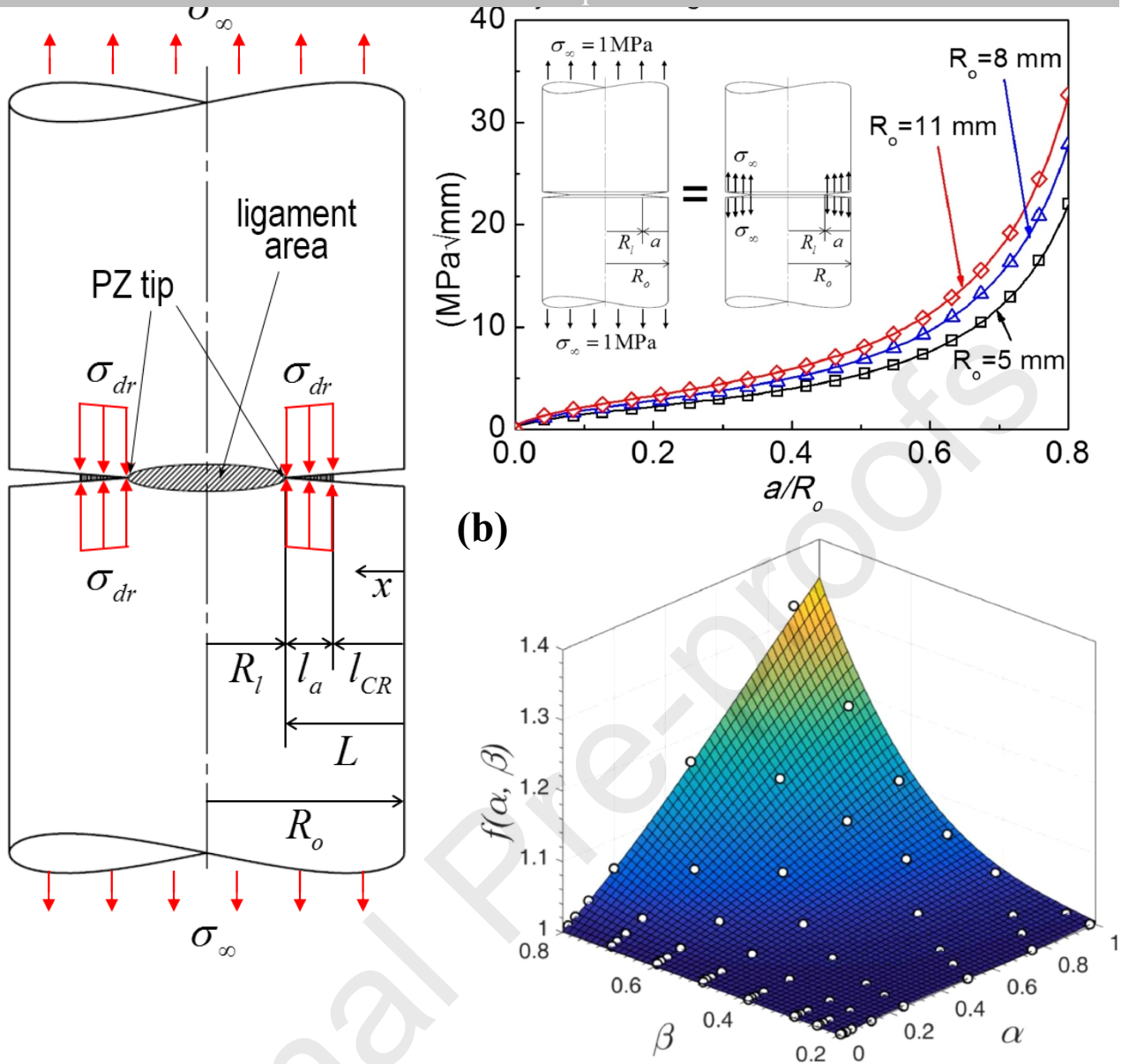


Fig. 8. (a) The configuration of the CRB specimen CL system with a wedge-like PZ, typically seen in HDPE. (b) A plot of the correction factor $f(\alpha, \beta)$ in the SIF Green's function G_{CRB}^{SIF} . The fit was carried using a 4th order bivariate polynomial, wherein the base data are displayed by white circle. (c) Comparison of the SIFs obtained from Wee et al. [38] Green's functions (GFs) for CRB specimen and Tada's handbook [69] at several a/R_o ratios and for $R_o = 5$ mm, $R_o = 8$ mm, and $R_o = 11$ mm. The applied stress is 1 MPa.

$$K_{CRB}^{Pa} = \int_0^L \frac{P_a}{\pi R_o^2} \cdot G_{CRB}^{SIF}(L, R_o; x) dx \quad (27)$$

where x is measured from the specimen's outer wall R_o . The above expression will be used to estimate the ERR induced by a single crack advancement J_I^{CR} . The pre-saturated PZ boundary traction is assumed constant and represented by the material's yield stress σ_y , which correspond to the PZ strain in the plasticized state. Therefore, the SIF due to shear yielding K_{CRB}^{Sy} , i.e., induced by the sorptive liquid plasticization, can be obtained by numerically integrating the GF of the CRB specimen, G_{CRB}^{SIF} , as follows:

$$K_{CRB}^{Sy} = -\sigma_y \int_{l_{CR}}^L G_{CRB}^{SIF}(L, R_o; x) dx \quad (28)$$

where σ_y is the HDPE pre-saturated yield stress. K_{CRB}^{Sy} is then used to estimate the ERR from single PZ advancement J_I^{PZ} . The total SIF K_{tot} is eventually calculated from the superposition of the SIF resulting from the axial load P_a and the yield stress σ_y , i.e., $K_{tot} = K_{\infty} + K_{Sy}$. The determination of the COD Green's functions is discussed next.

Table 1 C_i values of the fitted $f_i(a/W)$ functions for the CRB specimen using ninth order polynomial.

$f_i(\alpha)$	C_1	C_2	C_3	C_4	C_5	C_6	C_7	C_8	C_9
C_i	0.2188	0.131	-2.511	46.227	-	482.24	-	-	247.167
					198.32	0	568.031	568.031	
					5				

2.4.2 COD Green's function

The GF for the COD, $G_{CRB}^{COD}(a, R_o; x_1, x_0)$, stands for the COD developed at position x_1 by a unit circumferential force located at x_0 . The distances x_0 and x_1 are also measured from CRB specimen inner and outer surfaces. The $G_{CRB}^{COD}(a, R_o; x_1, x_0)$ can be established using Castigliano's theorem [69]. Let us set the actual force P_a that is applied at x_0 , and F as a circumferential fake force at x_1 . The ERR at the crack tip, i.e., $x = a$, can be calculated as $\frac{1}{E'}(K_P + K_F)^2 = \frac{1}{E'}(K_P^2 + 2K_P K_F + K_F^2)$. The partial derivative of ERR with respect to F , $\frac{\partial ERR}{\partial F}$, results in $\frac{1}{E'}(2K_P \frac{\partial K_F}{\partial F} + 2K_F \frac{\partial K_P}{\partial F})$. Considering the physical meaning of the ERR, and if we take the limits of $F \rightarrow 0$, and $K_F \rightarrow 0$, the COD at x_1 can be simplified as $COD(a, R_o; P_a; x_1, x_0) = \frac{2}{E'} \int_0^A K_P \frac{\partial K_F}{\partial F} dA$. The following expression of COD Green's function can be, hence, yielded by putting the circumferential applied load P_a as a unit ring force and considering $\frac{\partial K_F}{\partial F} = G_{CNB}^{SIF}(a, R_o; x_1)$ [70]:

$$G_{CRB}^{COD}(a, R_o; x_1, x_0) = \int_{max(x_0, x_1)}^a G_{CRB}^{SIF}(\xi, R_o; x_0) \cdot G_{CRB}^{SIF}(\xi, R_o; x_1) d\xi \quad (29)$$

$$\delta(a, R_o; x_1; \sigma(x_0)) = \int_0^a \sigma(x_0) G_{CRB}^{COD}(a, R_o; x_1, x_0) dx_0 \quad (30)$$

The total COD $\delta_{tot}(x)$ at position x and the total SIF at the PZ tip K_{tot} should, next, be obtained to compute X^L in Eq.(19). Both K_{tot} and $\delta_{tot}(x)$ can be considered as superposition of the remote stress σ_∞ and yield stress σ_y contributions:

$$K_{tot}(L, l_{CR}, R_o; \sigma_\infty, \sigma_{dr}) = \sigma_\infty \int_0^L G_{CRB}^{SIF}(L, R_o, x) dx - \sigma_y \int_{l_{CR}}^L G_{CRB}^{SIF}(L, R_o, x) dx \quad (31)$$

Similarly, $\delta_{tot}(x)$ can be computed as the superposition of the contribution of the remote stress COD $\delta_\infty(x)$ and the shear yielding COD $\delta_{sy}(x)$, i.e., $\delta_{tot}(x) = \delta_\infty(x) + \delta_{sy}(x)$, as follows:

$$\begin{cases} \delta_\infty(L, R_o; \sigma_\infty, \sigma_y; x) = \sigma_\infty \int_0^L G_{CRB}^{COD}(L, R_o; x, x_0) dx_0 \\ \delta_{sy}(L, l_{CR}, R_o; \sigma_\infty, \sigma_y; x) = -\sigma_y \int_{l_{CR}}^L G_{CRB}^{COD}(L, R_o; x, x_0) dx_0 \end{cases} \quad (32)$$

Consequently, for a given CL configurational lengths, l_{CR} and L , the PZ growth thermodynamic force X^L can be computed as constructed earlier in Eq.(19). The COD Green's function can now be used to compute the displacement of crack l_{CR} and crack layer L within the CRB specimen. The ERR calculated in section 2.4.1 reflects the strain energy physical change due to the SCG progression. The total displacement δ_{tot} can otherwise, using Castigliano theory, be determined directly [70]. Within a CRB geometry, the COD for a crack can accordingly be computed. The COD profile at the crack tip ($x_1 = l_{CR}$) can be evaluated for axial load P_a induced axial stress σ_a , through the double integration of the SIF Green's function over the crack face, as follows:

$$\delta_\infty = \frac{2\sigma_a}{E'} \int_x^{l_{CR}} \int_0^\xi G_{CRB}^{SIF}(\xi, R_o, R_i, x_0) \cdot G_{CRB}^{SIF}(\xi, R_o, R_i, x_1) dx_0 d\xi \quad (33)$$

where E' is the plain strain elastic modulus, x_0 is the location where the COD is measured, x_1 reflects the position where the unit force is applied, and ξ is the variable crack length. The shear yielding COD induced by the yield stress σ_y , is calculated in a similar way, as follows:

$$\delta_{sy} = -\frac{2\sigma_y}{E'} \int_x^L \int_{l_{CR}}^\xi G_{CRB}^{SIF}(\xi, R_o, R_i, x_0) \cdot G_{CRB}^{SIF}(\xi, R_o, R_i, x_1) dx_0 d\xi \quad (34)$$

The total COD δ_{tot} is then calculated by summing the COD due to axial load P_a and the yield stress σ_y , following the superposition principle, i.e., $\delta_{tot} = \delta_\infty + \delta_{sy}$. With that, the CL model simulation can be run and consequently its algorithm will be explained next.

2.5 Simulation algorithm of the CL model

The SFE, denoted as 2γ , is expected to decrease with time considering creep as the sole deformation mechanism at the crack tip and within the PZ. The PZ degradation is assumed to follow a creep damage, i.e., time-dependent deformation, that takes place within the drawn ligaments. By neglecting any dependency for the PZ state on its deformation history, the SFE reduction process can be expressed as $\gamma(t, t_x) = \gamma_0 \omega(t - t_x)$ [71]. Where ω is a function that decreases with time. With that, the PZ creep deformation can be reflected by defining the function ω as $\omega = \Omega(t - t_x)^{-1}$, where Ω

represents a creep function for the ligaments. The simplest expression in which the process of PZ fibers.

Considering hydrocarbon exposure, the HDPE degradation as outlined in section 2.3 will be, at each point x and time instance t , a function of plasticization damage $\omega(x,t)$ and a creep strain $\varepsilon^p(x,t)$. In continuous SCG, the ERR is higher than the initial SFE which would result in a positive crack driving force, i.e., no stationary state takes place with continuous crack advancement. As diffusion progresses and hydrocarbon saturation is not reached, the crack driving force increases and consequently the SCG rate, driven primarily by the chains lubrication and the resultant higher mobility. Once saturation is reached, the plasticization SFE $2\gamma_{plast}$ decays to the minimum level. This further reduces the initial SFE and consequently increases the SCG rate. The decay expressions of the SFE used are as follows, based on the material saturation state:

$$2\gamma(\omega(x,t),\varepsilon^p(x,t)) = 2\gamma_{mech} + 2\gamma_{plast} = 2\gamma_0 \left(\frac{1}{1 + \frac{t_i - t_x}{t^*}} + \left[\left(\frac{T_g(t)}{T_g(0)} \right)^n - 1 \right] \right) \quad (35)$$

where $2\gamma_0$ is undamaged material SFE, $2\gamma_{mech}$ is the mechanical SFE, $2\gamma_{plast}$ is the plasticization SFE, t^* is a characteristic time that impacts the speed of the decay, and t_x is the time of materials transformation at the point x calculated based on l_{CR} position with respect to l_{PZ} . $T_g(t)$ is the pre-saturated glass transition temperature, and $T_g(0)$ is the material undamaged value. The characteristic time, t^* , follows an Arrhenius type equation, $t^* = t_0 \exp(-J/RT)$ and strongly depends on temperature, where t_0 is a time scale, J is the activation energy of the process, R is the universal gas constant and T is temperature in Kelvin. The larger the t^* is, the slower the decay inside the PZ. In continuous SCG, no new thermodynamic equilibrium configuration is reached, and the crack and the PZ grow simultaneously with a positive crack driving. With that, to compute the crack and PZ growth rates, \dot{l}_{CR} and \dot{l}_{PZ} , the following relationships are used:

$$\dot{l}_{CR} = k_{CR}X^{CR}; \dot{l}_{PZ} = k_{PZ}X^{PZ} \quad (36)$$

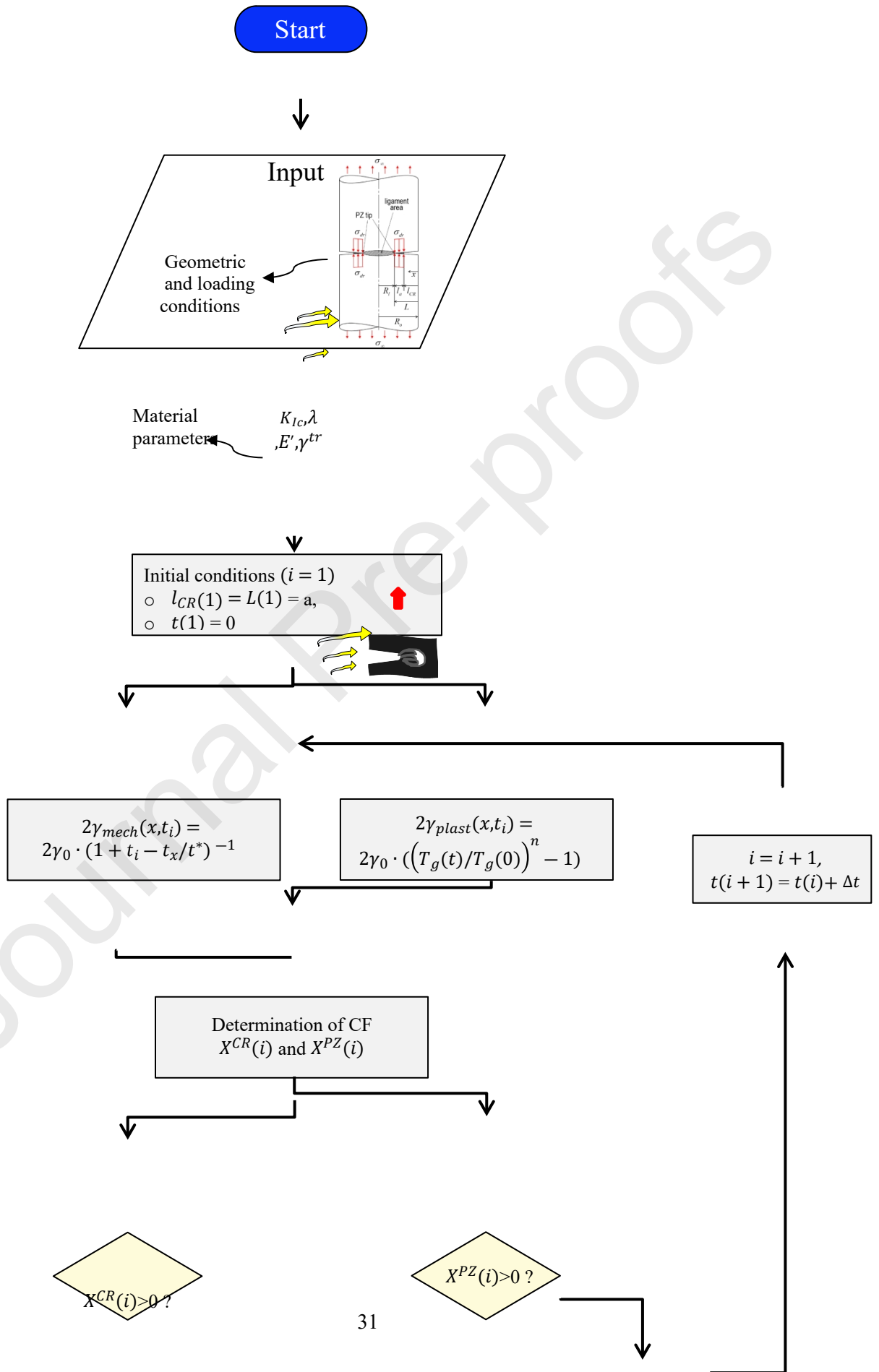
where \dot{l}_c and \dot{l}_p are the crack and PZ growth rates, respectively. Meanwhile, k_c and k_p are the crack and the PZ kinetic coefficients. The equations, despite their simple appearance, are non-linear systems and require numerical solvers. The crack keeps on growing until a local instability occurs and the SCG transforms to RCP. The algorithm of the CL system simulation is primarily made based on a loop statement along with multiple stages that dictate a single loop of calculation. For the i -th loop, the length of the crack $l_{CR}(i+1)$ and crack layer $L(i+1)$ are calculated using the following equations for a selected time increment Δt :

$$\begin{cases} l_{CR}(i+1) = l_{CR}(i) + \dot{l}_c(i) \cdot \Delta t \\ L(i+1) = L(i) + \dot{L}(i) \cdot \Delta t, \end{cases} \quad (37)$$

The crack and PZ evolution are calculated using Eq. (37). In the 1st stage of the loop, the initial SFE and the crack tip SFE are equal. Using the superposition method, the ERR $J_i^{PZ}(i)$, and the COD $\delta_\infty(i)$ at the PZ are calculated. The corresponding lengths would only change if the driving forces were positive. In the 2nd stage of the loop, 'i+1'-th loop, the crack tip SFE $\gamma(i+1)$ would change based on the numerical code. For example, if the new crack length $l_{CR}(i+1)$ was in between $l_{PZ}(i-2) \leq l_{CR}(i+1) < l_{PZ}(i-1)$, the SFE would be $\gamma_0 \cdot f(3dt)$. Similarly, if the new crack length was instead in between $l_{PZ}(i) \leq l_{CR}(i+1) < l_{PZ}(i+1)$, the SFE would be $\gamma_0 \cdot f(dt)$. Finally, if the new crack and PZ lengths are equal $l_{CR}(i+1) = l_{PZ}(i+1)$, the SFE goes back to the initial SFE $\gamma(i+1) = \gamma_0 \cdot f(0)$ whereby a fresh material is encountered.

In order to relate the physical SCG process in a CRB induced by a crack l_{CR} and the crack layer L , the CL continuous SCG mechanism is explained. The time elapsed from the test is denoted t . At $t = 0$, the crack length is a_0 , meanwhile the PZ develops at the crack tip. The crack would grow as long as the ERR at the tip is larger than the initial SFE γ_0 . The PZ does not reach equilibrium. Instead, the PZ keeps on decaying with the applied axial stress σ_a , which lead to the crack tearing the PZ area. Simultaneously, the PZ size increases, while the crack advances.

In the 3rd stage of the algorithm, two instability or failure criterion are used for terminating the simulation, as displayed in the last section of the algorithm flowchart in Fig 9. The 1st being the SIF exceeding the material fracture toughness, K_{Ic} . The 2nd being the remaining ligament exceeding the CRB thickness, t . Finally, once failure takes place, the crack l_{CR} and crack layer l lengths are plotted against time-to-failure t_f , as displayed in the output graph of Fig. 9. With that, the entire CL history can be seen.



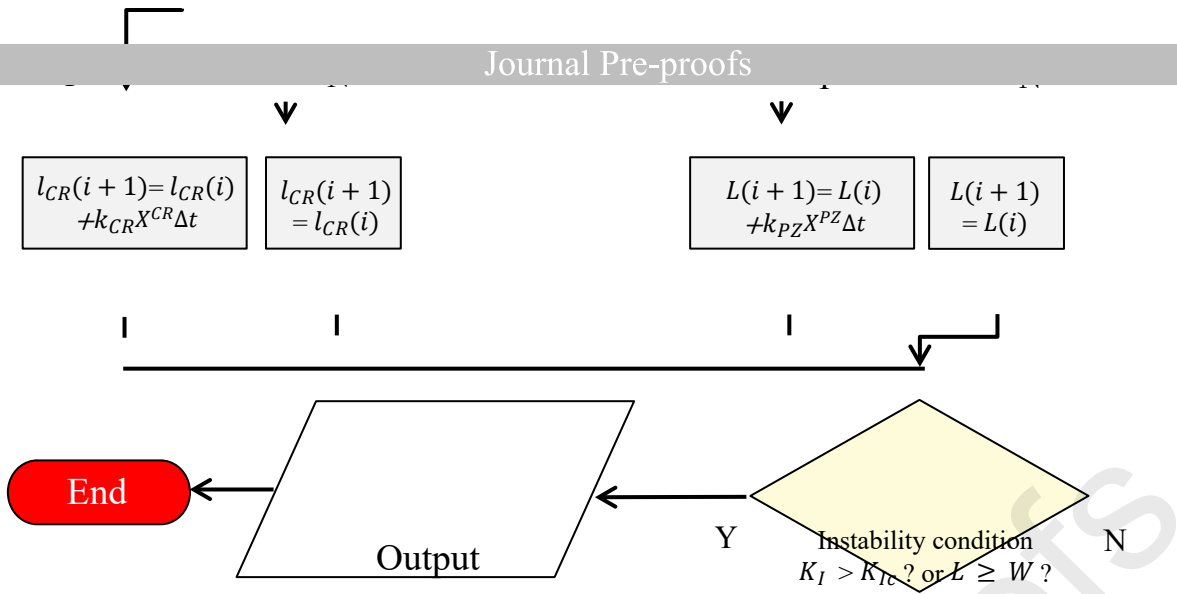


Fig. 9. Crack layer (CL) growth algorithm flowchart for the crack and crack layer, denoted l_{CR} and L , starting from the input geometry, loading and material parameters till the instability criterion. This includes the determination of the thermodynamic forces (TFs) for the crack X^{CR} and PZ X^{PZ} , separately. The crack instability is dedicated by either the applicable critical stress intensity factor (SIF) K_{IC} , i.e., fracture toughness, or the length of the remaining ligament L from the total width W .

3.1 Comparison with experiments

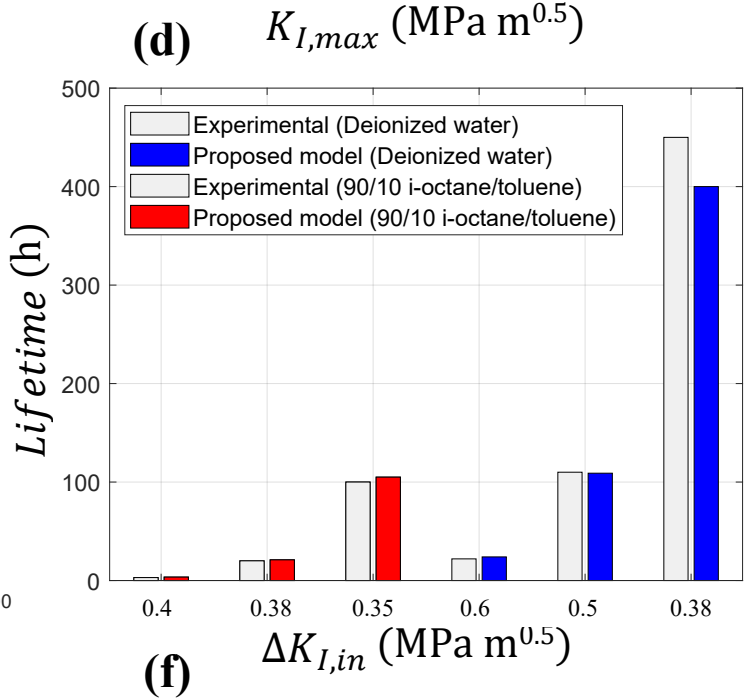
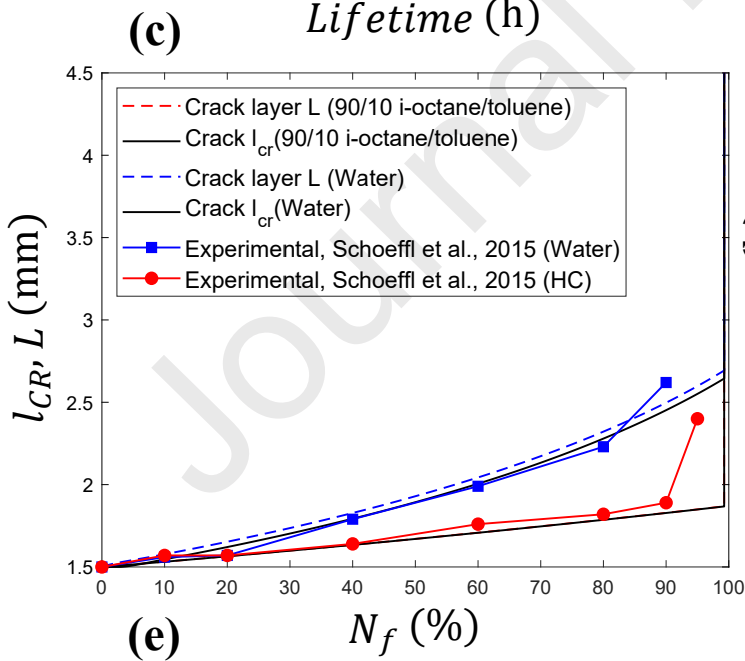
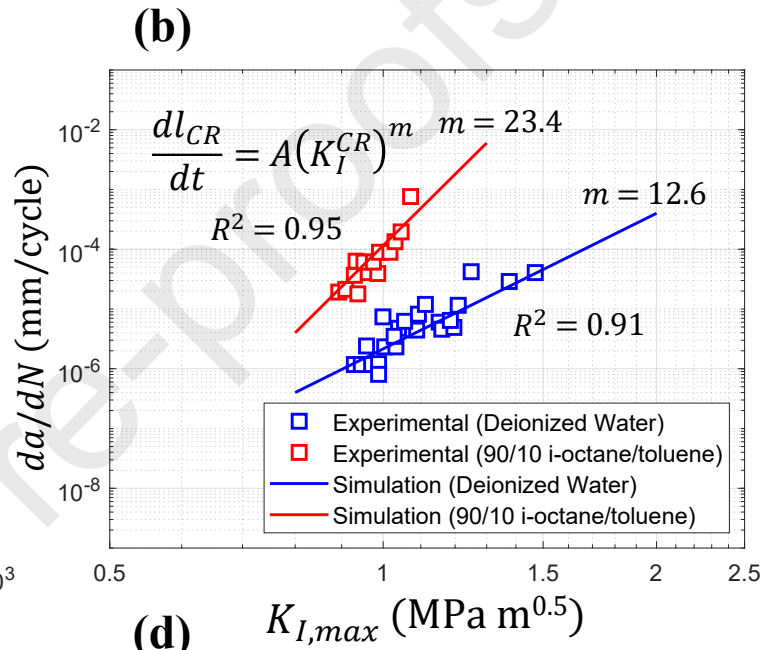
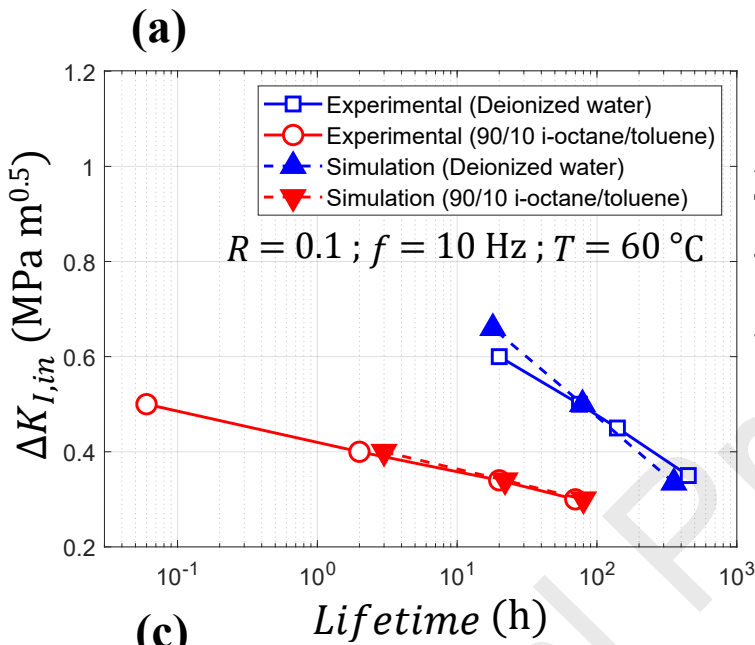
In this section, the proposed CL model is applied to a CRB specimen geometry made from HDPE. The CRB dimensions used in the simulations conform to ONR 25194 standard [72] with a 1.5 circumferential notch, 100 mm length, and a 13.85 mm diameter, which is currently replaced with ISO 18489 [73]. Schoeffl et al. [18], reported experimental SCG results for PE100 exposed to 90/10 wt% i-octane/toluene, using CRB specimens, under cyclic loading. A distinct continuous SCG kinetics with clear plasticization behavior were observed. The reported properties of the pre-saturated HDPE at $T = 60$ °C were adopted in the CL simulations, as shown in Table 2. The current CL model is applied to elevated temperatures by selecting the applicable material and physical properties at $T = 60$ °C.

The SCG response of the 90/10 wt% i-octane/toluene exposed specimens is compared to ones exposed to deionized water at $R = 0.1$; $f = 10$ Hz, as shown in Fig. 10(a). The crack growth rate da/dN versus the maximum SIF $K_{I,max}$, is plotted in Fig.10 (b). The SCG regime from the proposed CL model markedly agrees with the experimental rates from Schoeffl et al. [74]. The higher SCG rate of plasticized HDPE, with $m = 23.4$, can be simulated well compared to deionized water, with $m = 12.6$. The crack and crack layer lengths, l_{CR} and L , growth against the percentage of cycles to failure N_f , as shown in Fig. 10(c). Such additional simulations at pre-defined $\Delta K_{I,in}$ values that can achieve a total lifetime of approximately 2×10^6 cycles, which are 0.5 and 0.3 MPa $m^{0.5}$. The SCG of the plasticized HDPE is found to be almost linearly increasing up to 90%, with good agreement with the experiment, as shown in Fig. 10(d) and 10(e).

Table 2 The CL model material and physical input parameters for HDPE at $T = 60$ °C.

Description	Symbo l	Unit	Media exposed	
			0/10 wt% i-octane/toluen	Deionized water
Drawing stress, [75]	σ_{dr}	MPa	-	10
Yield stress, [18]	σ_y	MPa	11.4	14.8
Transformation energy per unit volume, [76]	γ^{tr}	mJ/m m ³	25	17
Initial surface fracture energy, [77]	γ_0	mJ/m m ²	20	15
Glass transition temperature, [62]	T_g	°C	-115	-
Saturated glass transition temperature, [62]	T_g^{sat}	°C	-79	-

Strain at yield, [78]	ε_0	-	2	-
Plane strain elastic modulus, [74, 75]	E'	MPa	385	500
Characteristic time, [34]	t^*	sec	300	300



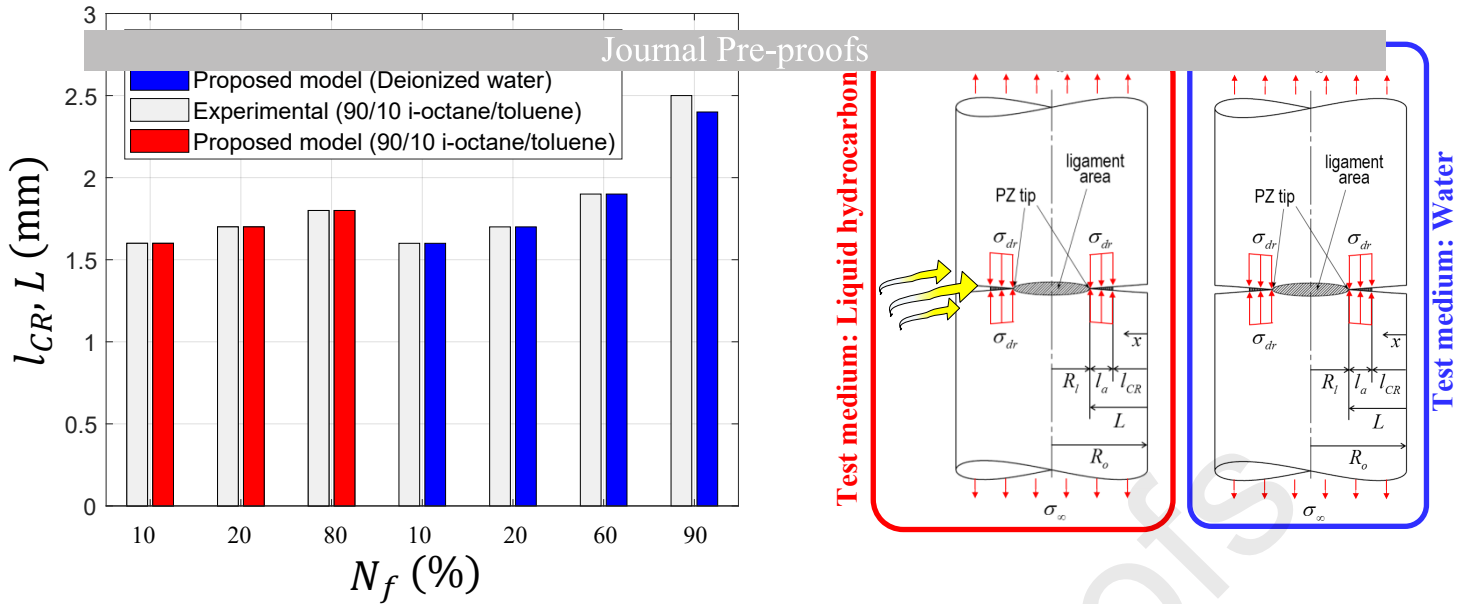


Fig. 10. (a) comparison of CL simulation results of SIF range ΔK_I versus failure time t_f , in deionized water and 90/10 wt% i-octane/toluene, at $R = 0.1$; $f = 10$ Hz; $T = 60$ °C. (b) Crack growth rate da/dN versus the maximum SIF $K_{I,max}$. The SCG regime from the proposed CL model markedly agrees with the experimental rates from Schoeffl et al. [74]. (c) Crack and crack layer lengths, l_{CR} and L , growth against the percentage of cycles to failure N_f . The present simulation results follow accurately the experimental t_f and l_{CR} from Schoeffl et al. [18], as shown in (d) and (e). A schematic illustration of the test CRB specimens in deionized water (blue) and 90/10 wt% i-octane/toluene (red), is shown in (f).

In this section, the CL model simulation is compared to the CRB fracture surface from Schoeffl et al. [18], that is exposed to 90/10 wt% i-octane/toluene. As shown in Fig. 11(b), a significant decrease in fibrillation can be seen in the SCG region driven primarily by the lubricative effect of the sorptive liquid to the inter-crystalline chains, similar to a stress cracking agent. This eventually promotes crystal slippage with no increase in the internal stress during plastic deformation within the PZ, i.e., shear yielding [68]. The tie-chains, i.e., inter-crystalline regions, within the lamella influence the mobility of the macromolecular network. The penetration of low molecular weight plasticizing fluids induces swelling of the HDPE amorphous phase and promotes a decline in the internal stresses [62].

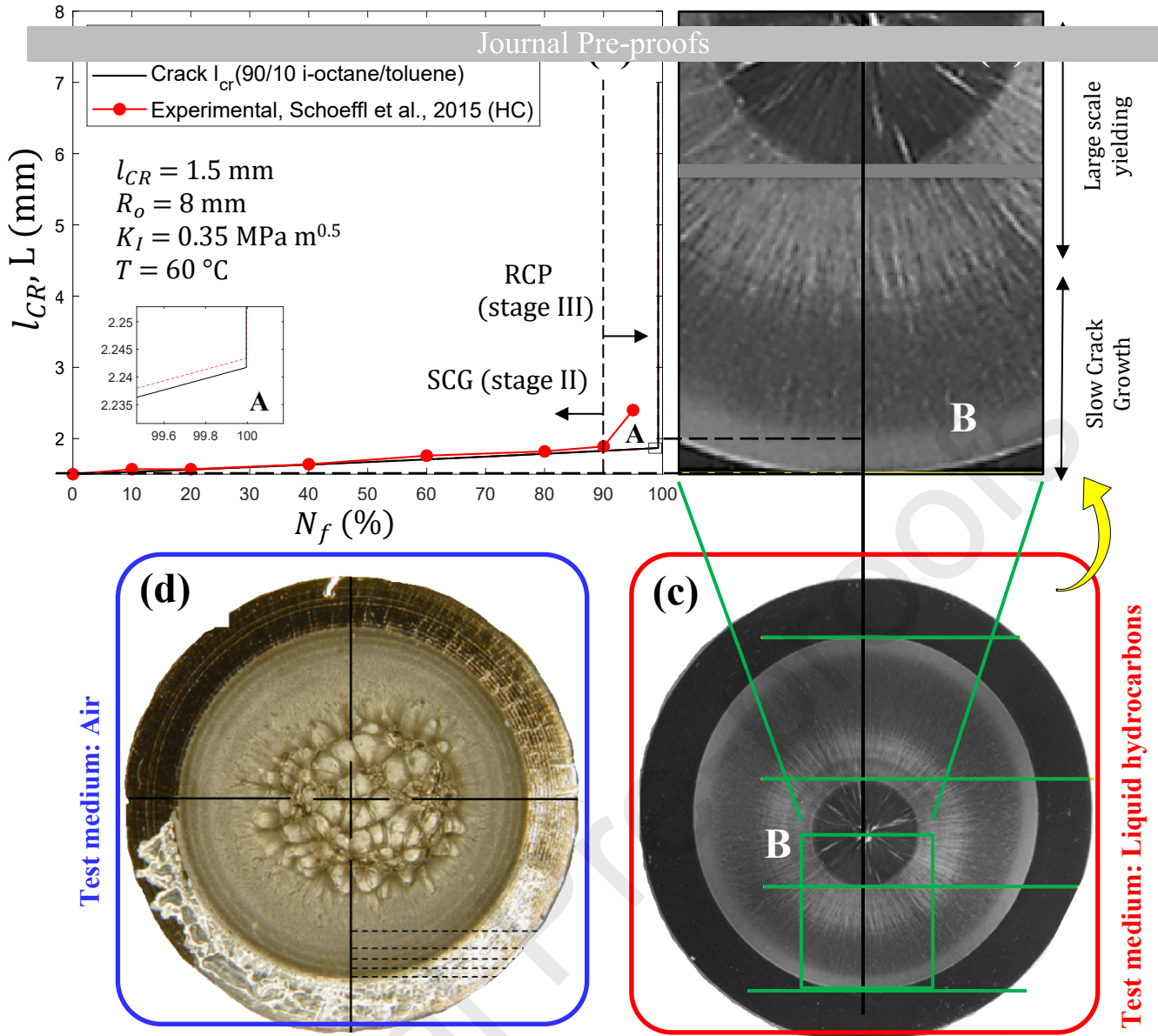
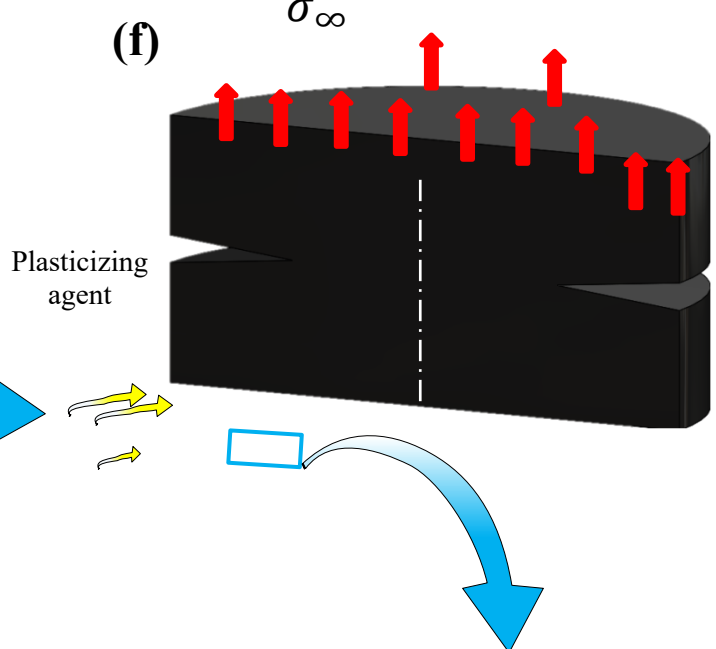
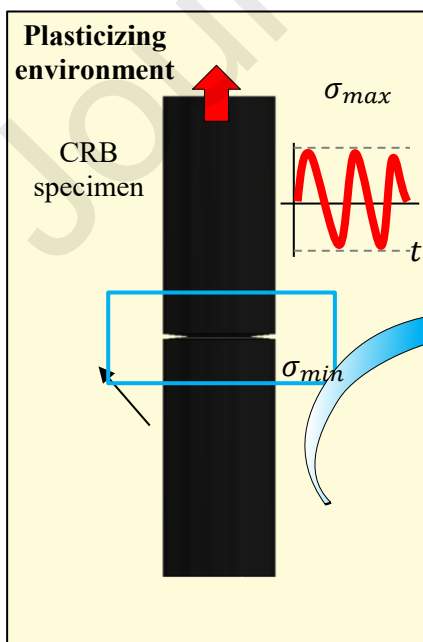
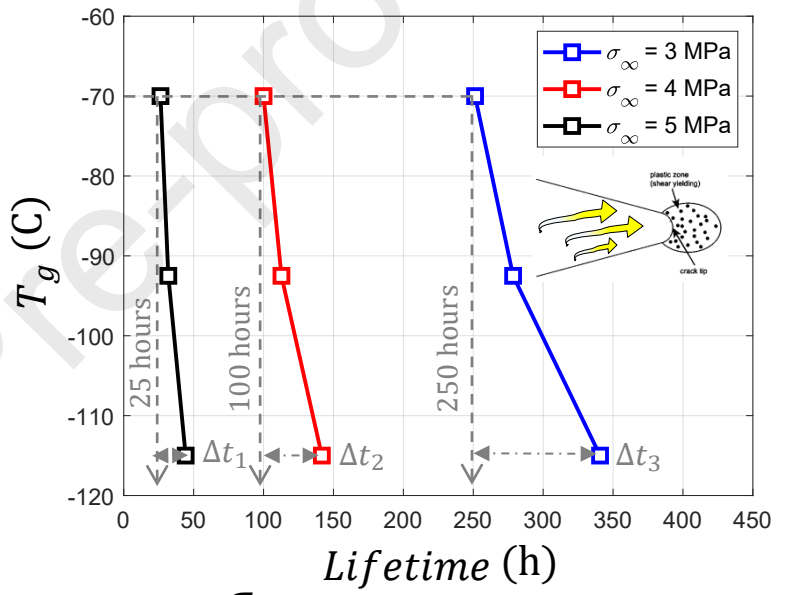
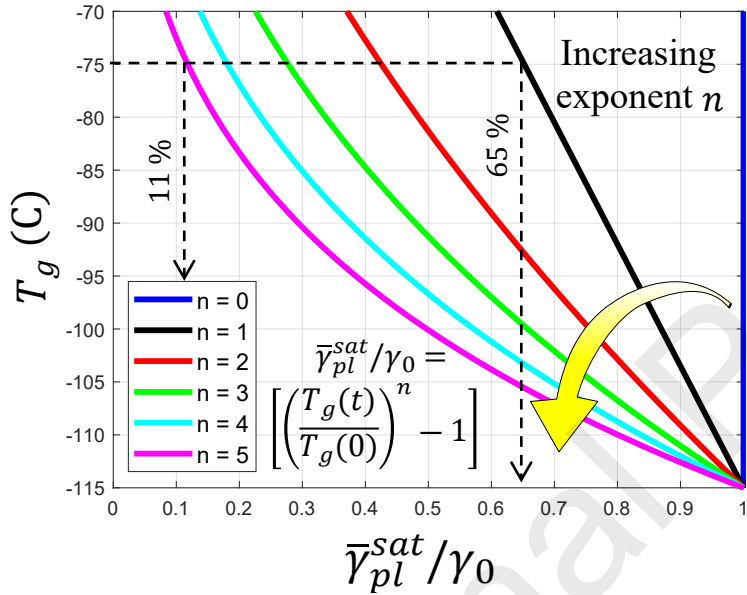
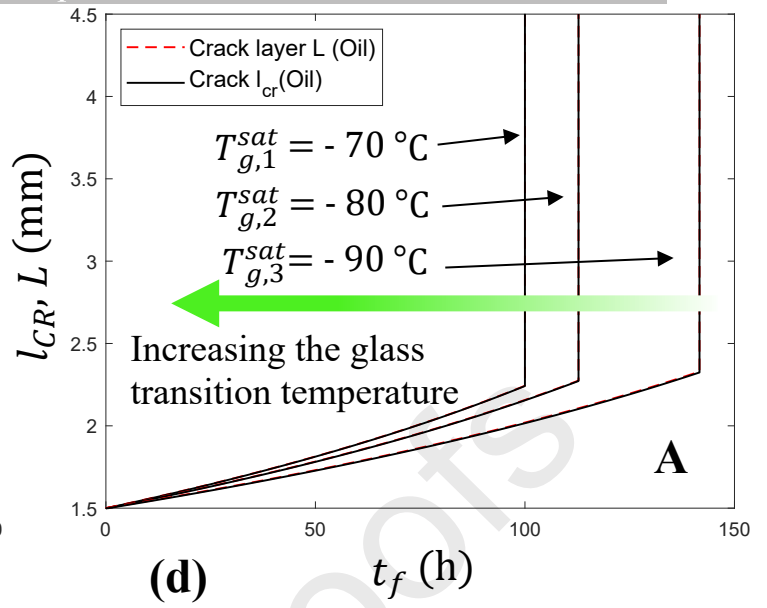
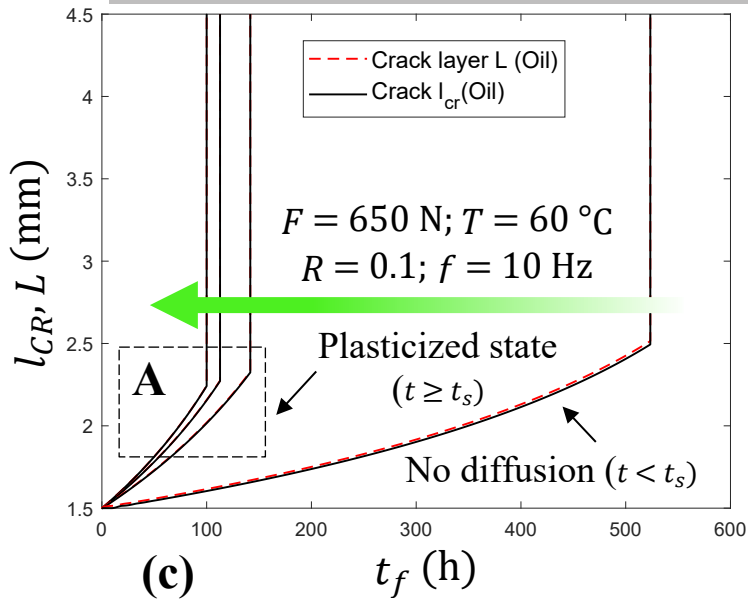


Fig. 11. Comparison of the crack and crack layer lengths, l_{CR} and L , growth from (a) the CL simulation and the fracture surface in (b), at $K_I = 0.35$ MPa $m^{0.5}$, and $T = 60$ °C. The SCG and large-scale yielding regimes are highlighted along with the growth increments of l_{CR} and L (dashed black). (c) A macroscopic view of the CRB fracture surface, that is tested in 90/10 wt% i-octane/toluene, from the magnified view in (b), and boxed in yellow. (d) A CRB specimen fracture surface exposed to deionized water. The discontinuous SCG striations seen in (d) are not visible in (c) air from Pinter et al. [79] owing to the deformation mechanism change from craze breakdown to PZ tearing induced by plasticization.

3.2 Parametric study

In this section, two example cases are presented to validate the feasibility of the proposed CL model. The SCG behavior of plasticized HDPE is investigated using CRB specimens and under fatigue loading, and at elevated temperature, $T = 60$ °C. A specimen with a radius, R , of 7 mm, and an initial notch l_0 of 1.5 mm is used. A maximum force F of 650 N is applied, corresponding to a maximum stress σ_{max} of 4 MPa, with $R = 0.1$, and $f = 10$ Hz. The material and physical properties listed in Table 2, of HDPE pre-saturated in 90/10 wt% i-octane/toluene, are used as input parameters for the CL

The simulations were performed for various pre-saturated conditions, including non-plasticized HDPE, as shown in Fig. 2(a), from right to left. Since no diffusion has occurred at $t < t_s$, no plasticization damage would take place within the PZ. Consequently, the SFE 2γ would be governed by the creep strain $\varepsilon^p(x,t)$, resulting in a longer failure time t_f . Once the sorptive liquid reach complete diffusion and saturation takes place, $t \geq t_s$, a plasticized state governs the material response. This activates the plasticization damage $\omega(x,t)$ within the SFE 2γ , and results in an acceleration of the SCG process, as shown in Fig.12(a). Apparently, the PZ deformation of HDPE, being a semicrystalline polymer, is not only constituted by the crystalline lamellae, but also by the diffusion of such sorptive liquid into its amorphous phase, filling the free volume pores [62, 80]. The same is justified by the different yield σ_y stress for materials with identical crystallinity, and the rise in yield stress σ_y by annealing with limited change in HDPE crystal structure. A magnified view of the crack and crack layer growth, l_{CR} and L , at three saturated glass transition temperature T_g^{sat} values, i.e., $T_{g,i}^{sat} = -70$ °C, -80 °C, and -90 °C, is shown in Fig. 12(b). As can be seen, the higher T_g^{sat} , the higher $\omega(x,t)$ is and the lower t_f is. The material transitions from a glassy state to rubbery state. The introduction of plasticizers molecules leads to a higher extent of chains mobility based on the rise of HDPE T_g towards a higher value, i.e., $T_{g,1}^{sat} > T_{g,2}^{sat} > T_{g,3}^{sat}$.



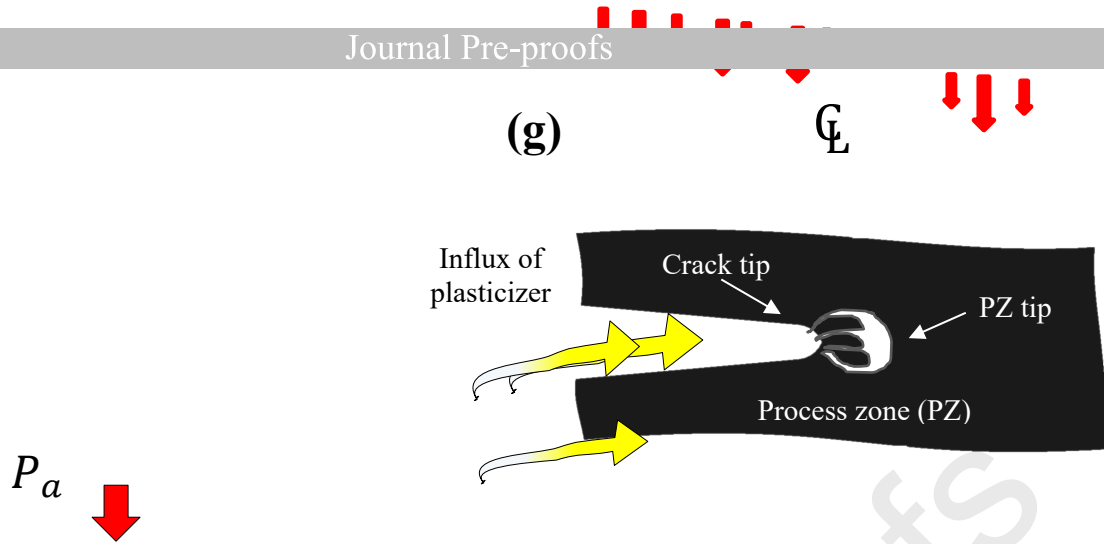


Fig. 12. The parametric simulation results of the proposed CL model for various T_g conditions. (a) Crack and crack layer, l_{CR} and L , propagation with various glass transition temperature values at $R = 0.1$, $f = 10$ Hz, $T = 60$ °C ; $F = 650$ N. (b) magnified view of region ‘A’ showing l_{CR} and L growth at $T_{g,i}^{sat} = -70$ °C, -80 °C, and -90 °C. (c) variation of the normalized plasticization surface fracture energy (SFE) $\bar{\gamma}_{pl}^{sat}/\gamma_0$ with the glass transition temperature T_g , for various exponent n levels. (d) effect of T_g variation on the lifetime at different applied stress levels, namely $\sigma_{Pa} = 3$ MPa, 4 MPa, and 5 MPa. (e) a schematic representation of the CRB specimen immersed in a plasticizing environment. (f) Diffusion of the plasticizing agent into the PZ by absorption. (c) Magnified view of the influx of the plasticizing agent at the crack tip.

For hydrocarbons with larger plasticization effect, the exponent n within the saturated SFE $\bar{\gamma}_{pl}^{sat}$ can be adjusted to account for the dependency on T_g . For instance, for a PE material with a T_g of -115 °C and T_g^{sat} of -75 °C, the drop in $\bar{\gamma}_{pl}^{sat}$, by increasing the exponent n from $n = 0$ to $n = 5$, can vary from 65% down to 11% from the initial SFE γ_0 , as outlined in Fig. 12(c). Physically, with this change, the macromolecular chains in the amorphous phase are further stretched by the infusion of this stronger plasticizer, generating higher uniaxial stress that acts on the lamellae surfaces. The amorphous phase, consequently, is subjected to a larger uniaxial tension transmitted to the crystal surfaces. The presence of such more penetrable molecules makes the retraction of the amorphous phase impossible due to osmotic pressure and macromolecules connecting adjacent lamellae being stretched.

The effect of the variation of T_g for various applied stresses σ_{Pa} is shown in Fig. 12(d). The lifetime is simulated for three applied stress levels σ_{Pa} , namely 3 MPa, 4 MPa, and 5 MPa. This was carried for the same PE material with T_g of -115 °C and T_g^{sat} of -70 °C. The lifespan, for the plasticized state, is found to drop from 250 hours at $\sigma_{Pa} = 3$ MPa, to 100 hours at $\sigma_{Pa} = 4$ MPa, and eventually to 25 hours at $\sigma_{Pa} = 5$ MPa, representing a 60 % and a 90 % decline, respectively. On the other hand, for the non-plasticized state, with $T_g = -115$ °C, the lifetime variation is found to be more sensitive than in the plasticized state. The lifespan is found to drop 58 % from $\sigma_{Pa} = 4$ MPa to $\sigma_{Pa} = 3$ MPa, and 87 % from $\sigma_{Pa} = 5$ MPa to $\sigma_{Pa} = 3$ MPa. The lifetime variation is also found to be more sensitive at higher stresses, e.g., $\sigma_{Pa} = 3$ MPa, than at lower levels, e.g., $\sigma_{Pa} = 3$ MPa, comparing plasticized HDPE, at T_g of -70 °C, and neat HDPE, at $T_g = -115$ °C. In other words, Δt_1 increase is found to be approximately 70%, whereas Δt_2 and Δt_3 drops to nearly 42 % and 35 %, respectively.

Such insights can aid in the assessments of many industrial and design applications, enabling the

[81]. This effect, though, can be accounted for in the future, as reported by Jones et al. [81], using the Simple Scaling approach that was first proposed to metal [82], and the Hartman-Schijve variant of the Nasgro crack growth equation [83]. As shown by Jones et al. [81], the Hartman–Schijve crack growth equation was able to account for the differences in the crack growth rate, da/dt , versus ΔK curves for three different HDPE compositions, demonstrating its success in analysing the SCG rate for various HDPE grades.

4. Conclusions and future perspectives

In this study, a novel simulation framework was proposed by developing a fundamental model for the diffusion-assisted SCG behavior of HDPE exposed to a plasticizing fluid, e.g., hydrocarbons. When a polymeric material is in contact with such sorptive liquids, it is commonly observed that the deformation mechanism within the PZ switches from craze breakdown to shear yielding. Owing to such changes in the PZ deformation, the plasticized behavior of the PZ should be modeled with a mechanistic approach. Kinetic equations for the deterioration of the PZ surface fracture energy are proposed. In addition, the Green's function for stress intensity factor (SIF) was developed to analyze the released energy with cracking for an axisymmetric solid. A parametric study of several input parameters, such as the glass transition temperature T_g and the applied stress σ_{Pa} , was conducted to examine whether the developed model revealed appropriate trends. Using the proposed model, the reported plasticization results were reconstructed successfully, including the cycles to failure N_f , crack evolution length l_{CR} the SCG rate with $R^2 = 0.95$.

In the future, additional investigations can be done in order to improve the developed CL model predictions. For example: 1) hydrocarbon-based plasticizers, which are well-known sorptive liquids that attack the HDPE pipe, are commonly encountered in various chemical forms, for example, sent oils or gaseous fuels. There are several steps in the physical and chemical reaction mechanism and kinetics of these chemicals. In this study, however, it is assumed that one type of plasticizers diffuses into the polymer substance and is consumed as it is, through an irreversible chemical reaction. 2) The chemical reaction and the washing out of the anti-oxidants (AO) from the specimen outer wall was not considered. Therefore, the process of AO and stabilizer extraction and chemical aging from the absorption of hydrocarbons can be considered in future works.

Nevertheless, this study outcomes are significant as they provide a fundamental mechano-chemical degradation model that enables the understanding of plasticization failure behaviors from actual oilfield sites. In addition, it is a newly proposed framework for thermoplastics lifetime assessments in the plasticized state, wherein the damage parameter can be physically estimated. These results revealed the tendency of SCG acceleration and independence of the lifetime from the applied stress in the highly plasticized condition, which has only been characterized as a phenomenological method. All in all, the lifespan and reliability of HDPE pipes under plasticizing environments can be accurately predicted, given that few input parameters are determined with small-scale tests.

Acknowledgement

The authors would like to acknowledge UAE University for providing the facilities and funds through Materials library (#31N392) - Industry 4.0 district project.

References

2. Hutař, P., et al., *A numerical methodology for lifetime estimation of HDPE pressure pipes*. Engineering Fracture Mechanics, 2011. **78**(17): p. 3049-3058.
3. Nasiri, S. and M.R. Khosravani, *Failure and fracture in polyethylene pipes: Overview, prediction methods, and challenges*. Engineering Failure Analysis, 2023: p. 107496.
4. Shi, J., et al., *Evaluation of the seismic performance of butt-fusion joint in large diameter polyethylene pipelines by full-scale shaking table test*. Nuclear Engineering and Technology, 2023.
5. Favier, V., et al., *Slow crack propagation in polyethylene under fatigue at controlled stress intensity*. Polymer, 2002. **43**(4): p. 1375-1382.
6. Plummer, C.J.G., A. Goldberg, and A. Ghanem, *Micromechanisms of slow crack growth in polyethylene under constant tensile loading*. Polymer, 2001. **42**(23): p. 9551-9564.
7. Deblieck, R.A.C., et al., *Failure mechanisms in polyolefines: The role of crazing, shear yielding and the entanglement network*. Polymer, 2011. **52**(14): p. 2979-2990.
8. Almomani, A., et al., *Constitutive model calibration for the thermal viscoelastic-viscoplastic behavior of high density polyethylene under monotonic and cyclic loading*. Polymer Testing, 2022: p. 107911.
9. Rahman, S.M., T. Hassan, and E. Corona, *Evaluation of cyclic plasticity models in ratcheting simulation of straight pipes under cyclic bending and steady internal pressure*. International Journal of Plasticity, 2008. **24**(10): p. 1756-1791.
10. El-Sayed, M., et al., *Leak before break fracture assessment of pressurized unplasticized PVC pipes with axial surface crack: Experimental and analytical analysis*. Engineering Fracture Mechanics, 2022. **266**: p. 108394.
11. Ritums, J.E., et al., *Mechanical properties of high-density polyethylene and crosslinked high-density polyethylene in crude oil and its components*. Journal of Polymer Science Part B: Polymer Physics, 2006. **44**(4): p. 641-648.
12. Böhning, M., et al., *Impact of biodiesel sorption on mechanical properties of polyethylene*. Polymer testing, 2014. **34**: p. 17-24.
13. Erdmann, M., M. Böhning, and U. Niebergall, *Physical and chemical effects of biodiesel storage on high-density polyethylene: Evidence of co-oxidation*. Polymer Degradation and Stability, 2019. **161**: p. 139-149.
14. Böhning, M., et al., *Impact of biodiesel sorption on tensile properties of PE-HD for container applications*. Polymer Testing, 2016. **50**: p. 315-324.
15. Schilling, M., et al., *Relation of craze to crack length during slow crack growth phenomena in high-density polyethylene*. Polymer Engineering & Science, 2024.
16. Deveci, S., et al., *Creep rupture of plastic pipes: Effect of eccentricity, residual stress, and circumferential orientation*. Polymer Testing, 2024: p. 108408.
17. Gao, B., et al., *Fatigue crack growth and slow crack growth of HDPE pipes under internal pressure and flat plate compression*. International Journal of Pressure Vessels and Piping, 2024: p. 105155.
18. Schoeffl, P.F. and R.W. Lang, *Effect of liquid oilfield-related media on slow crack growth behavior in polyethylene pipe grade materials*. International Journal of Fatigue, 2015. **72**: p. 90-101.
19. Schilling, M., *Environmental Stress Cracking (ESC) and Slow Crack Growth (SCG) of PE-HD*

20. Schilling, M., et al., *Environmental stress cracking of polyethylene high density (PE-HD) induced by liquid media—Validation and verification of the full-notch creep test (FNCT) Umgebungsinduzierte Spannungsrisssbildung von Polyethylen-Werkstoffen hoher Dichte durch flüssige Medien—Validierung und Verifizierung des Kriechversuchs an Probekörpern mit umlaufender Kerbe*. Materialwissenschaft und Werkstofftechnik, 2017. **48**(9): p. 846-854.
21. Wee, J.W., Y. Zhao, and B.H. Choi, *Observation and modeling of environmental stress cracking behaviors of high crystalline polypropylene due to scent oils*. Polymer Testing, 2015. **48**: p. 206-214.
22. Nguyen, K.Q., et al., *Long-term testing methods for HDPE pipe—advantages and disadvantages: a review*. Engineering Fracture Mechanics, 2021. **246**: p. 107629.
23. 4437, I., *plastics piping systems for the supply of gaseous fuels – polyethylene (PE)* 2024. p. 20.
24. 4433, I., *Thermoplastics pipes Resistance to liquid chemicals Classification Part I: Immersion test method*. 1997. p. 13.
25. Mourad, A.-H.I., A. El-Domiati, and Y.J. Chao, *Fracture toughness prediction of low alloy steel as a function of specimen notch root radius and size constraints*. Engineering Fracture Mechanics, 2013. **103**: p. 79-93.
26. Thuy, M., et al., *Environmental Stress Cracking of High-Density Polyethylene Applying Linear Elastic Fracture Mechanics*. Polymers, 2022. **14**(12): p. 2415.
27. Kamaludin, M.A., et al., *A fracture mechanics approach to characterising the environmental stress cracking behaviour of thermoplastics*. Theoretical and Applied Fracture Mechanics, 2017. **92**: p. 373-380.
28. Alavi, S.M. and M.T. Kazemi, *Cohesive crack growth in polyethylene considering Schapery equation using XFEM*. International Journal of Mechanical Sciences, 2024. **263**: p. 108759.
29. Aydiner, I.U., B. Tatli, and T. Yalçinkaya, *Investigation of failure mechanisms in dual-phase steels through cohesive zone modeling and crystal plasticity frameworks*. International Journal of Plasticity, 2024: p. 103898.
30. Zhang, Q., Z. Xu, and W. Tao, *Rate dependent cohesive zone model for fatigue crack growth*. International Journal of Mechanical Sciences, 2024: p. 109144.
31. Wang, H., et al., *The roles of cohesive strength and toughness for crack growth in visco-elastic and creeping materials*. Engineering Fracture Mechanics, 2016. **160**: p. 226-237.
32. Gong, Y., et al., *A modified mode I cohesive zone model for the delamination growth in DCB laminates with the effect of fiber bridging*. International Journal of Mechanical Sciences, 2020. **176**: p. 105514.
33. Chudnovsky, A., *Crack layer theory*. 1984: The Center.
34. Almomani, A., A.-H.I. Mourad, and S. Deveci, *Effect of the crack layer theory parameters on the discontinuous slow crack growth of high density polyethylene under fatigue loading*. International Journal of Solids and Structures, 2024. **286**: p. 112579.
35. Papenfuß, C., *Continuum thermodynamics and constitutive theory*. 2020: Springer.
36. Chudnovsky, A. and A. Moet, *Thermodynamics of translational crack layer propagation*. Journal of materials science, 1985. **20**(2): p. 630-635.
37. Sehanobish, K., et al., *An analysis for crack layer stability*. International journal of fracture, 1986. **32**:

38. Wee, J.W. and B.H. Choi, *Modeling of axisymmetric slow crack growth of high-density polyethylene with circular notched bar specimen using crack layer theory*. International Journal of Solids and Structures, 2016. **97_98**: p. 189-199.
39. Zhang, H., Z. Zhou, and A. Chudnovsky, *Applying the crack-layer concept to modeling of slow crack growth in polyethylene*. International Journal of Engineering Science, 2014. **83**: p. 42-56.
40. Almomani, A. and A.-H.I. Mourad, *The fracture toughness of Schwarz Primitive triply periodic minimal surface lattice*. Theoretical and Applied Fracture Mechanics, 2023. **125**: p. 103924.
41. Almomani, A. and A.-H.I. Mourad, *Crack layer modeling of butt-fusion joints induced slow crack growth in high-density polyethylene pipes*. International Journal of Solids and Structures, 2024: p. 112970.
42. Choi, B.H., et al., *Experimental and theoretical investigation of stress corrosion crack (SCC) growth of polyethylene pipes*. Polymer Degradation and Stability, 2009. **94**(5): p. 859-867.
43. Khaleghi, H., A. Amiri-Rad, and M. Mashayekhi, *A thermodynamically consistent continuum damage model for time-dependent failure of thermoplastic polymers*. International Journal of Plasticity, 2022. **154**: p. 103278.
44. Almomani, A., A.-H.I. Mourad, and I. Barsoum, *Effect of sulfur, phosphorus, silicon, and delta ferrite on weld solidification cracking of AISI 310S austenitic stainless steel*. Engineering Failure Analysis, 2022: p. 106488.
45. Shojaei, A., G.Z. Voyiadjis, and P.J. Tan, *Viscoplastic constitutive theory for brittle to ductile damage in polycrystalline materials under dynamic loading*. International Journal of Plasticity, 2013. **48**: p. 125-151.
46. Bouvard, J.-L., et al., *An internal state variable material model for predicting the time, thermomechanical, and stress state dependence of amorphous glassy polymers under large deformation*. International Journal of Plasticity, 2013. **42**: p. 168-193.
47. Almomani, A.F., H. Alhaj, and A.-H. Ismail Mourad. *The Influence of Low Melting Point Elements on Hot-Cracking of 310 Austenitic Stainless Steel*. American Society of Mechanical Engineers.
48. Almomani, A.F., H. Alhaj, and A.-H. Ismail Mourad. *The Impact of Silicon Content on the Corrosion Resistance of Nickel-Molybdenum Alloy in High Concentration Sulfuric Acid Transport*. American Society of Mechanical Engineers.
49. Mourad, A.-H.I., et al., *Failure analysis of gas and wind turbine blades: A review*. Engineering Failure Analysis, 2023. **146**: p. 107107.
50. (ASTM), A.S.f.T.a.M., *Standard Test Method for Measurement of Fatigue Crack Growth Rates*, in *ASTM E647-23a*. ASTM.
51. Balieu, R., et al., *A fully coupled elastoviscoplastic damage model at finite strains for mineral filled semi-crystalline polymer*. International Journal of plasticity, 2013. **51**: p. 241-270.
52. Krairi, A. and I. Doghri, *A thermodynamically-based constitutive model for thermoplastic polymers coupling viscoelasticity, viscoplasticity and ductile damage*. International Journal of Plasticity, 2014. **60**: p. 163-181.
53. Wang, J., et al., *A finite strain thermodynamically-based constitutive modeling and analysis of viscoelastic-viscoplastic deformation behavior of glassy polymers*. International Journal of Plasticity, 2019. **122**: p. 135-163.

55. De Groot, S.R. and P. Mazur, *Non-equilibrium thermodynamics*. 2013: Courier Corporation.
56. Chudnovsky, A., *Crack layer theory*. 1984: p. NASA report, N174634.
57. Onsager, L., *Reciprocal relations in irreversible processes. I*. Physical Review, 1931. **37**(4): p. 405.
58. Choi, B.H., et al., *The use of crack layer theory to predict the lifetime of the fatigue crack growth of high density polyethylene*. Polymer Engineering & Science, 2009. **49**(7): p. 1421-1428.
59. Eshelby, J., *Energy relations and the energy-momentum tensor in continuum mechanics*, in *Fundamental Contributions to the Continuum Theory of Evolving Phase Interfaces in Solids*. 1999, Springer. p. 82-119.
60. Parsons, M., et al., *Effect of strain rate on stepwise fatigue and creep slow crack growth in high density polyethylene*. Journal of materials science, 2000. **35**(8): p. 1857-1866.
61. Stojimirovic, A., K. Kadota, and A. Chudnovsky, *An equilibrium process zone in polymeric materials*. Journal of applied polymer science, 1992. **46**(6): p. 1051-1056.
62. Rozanski, A. and A. Galeski, *Plastic yielding of semicrystalline polymers affected by amorphous phase*. International journal of plasticity, 2013. **41**: p. 14-29.
63. Ueberreiter, K. and G. Kanig, *Self-plasticization of polymers*. Journal of Colloid Science, 1952. **7**(6): p. 569-583.
64. Sun, F., et al., *Molecular-level investigation of plasticization of polyethylene terephthalate (PET) in supercritical carbon dioxide via molecular dynamics simulation*. Royal Society Open Science, 2022. **9**(8): p. 220606.
65. Böhning, M., et al., *Influence of biodiesel sorption on temperature-dependent impact properties of polyethylene*. Polymer testing, 2014. **40**: p. 133-142.
66. Chen, D. and H.G. Zachmann, *Glass transition temperature of copolyesters of PET, PEN and PHB as determined by dynamic mechanical analysis*. Polymer, 1991. **32**(9): p. 1612-1621.
67. Pradhan, D.K., et al., *Effect of plasticizer on structure—property relationship in composite polymer electrolytes*. Journal of power sources, 2005. **139**(1-2): p. 384-393.
68. Saad, A.K., F.P.C. Gomes, and M.R. Thompson, *Plasticizing effect of oxidized biodiesel on polyethylene observed by nondestructive method*. Fuel, 2019. **252**: p. 246-253.
69. Tada, H., P. Paris, and G. Irwin, *The stress analysis of cracks handbook, 3rd ed.* 2000, New York: ASME Press.
70. Kadota, K. and A. Chudnovsky, *Constitutive equations of crack layer growth*. Polymer Engineering & Science, 1992. **32**(16): p. 1097-1104.
71. Chudnovsky, A. and Y. Shulkin, *Application of the crack layer theory to modeling of slow crack growth in polyethylene*. International Journal of Fracture, 1999. **97**(1-4): p. 83-102.
72. 25194, O., *Determination Of The Resistance To Slow Crack Growth Of Polyethylene With Cracked Round Bar (CRB) Specimens*. 2011, Austrian Standards International. p. 13.
73. ISO, *Polyethylene (PE) materials for piping systems — Determination of resistance to slow crack growth under cyclic loading — Cracked Round Bar test method*, in *ISO 18489*. 2015, ISO.

75. Shahin, A., I. Barsoum, and M.D. Islam, *Constitutive model calibration of the time and temperature-dependent behavior of high density polyethylene*. Polymer Testing, 2020. **91**.
76. Chudnovsky, A., et al., *Lifetime assessment of engineering thermoplastics*. International Journal of Engineering Science, 2012. **59**: p. 108-139.
77. Wee, J.-W., A. Chudnovsky, and B.-H. Choi, *Crack layer modeling of overload-induced slow crack growth retardation of high-density polyethylene*. International Journal of Mechanical Sciences, 2023: p. 108546.
78. Wiley, K. and E. Lever, *Effects of Hydrocarbon Permeation on Plastic Pipe Strength and Fusion Performance*. 2015.
79. Pinter, G., et al., *Cyclic crack growth tests with CRB specimens for the evaluation of the long-term performance of PE pipe grades*. Polymer Testing, 2007. **26**(2): p. 180-188.
80. Rozanski, A. and A. Galeski, *Controlling cavitation of semicrystalline polymers during tensile drawing*. Macromolecules, 2011. **44**(18): p. 7273-7287.
81. Jones, R., A.J. Kinloch, and A.S.M. Ang, *Modelling Fatigue Crack Growth in High-Density Polyethylene and Acrylonitrile Butadiene Styrene Polymers*. Polymers, 2024. **16**(9): p. 1299.
82. Schönbauer, B.M., et al., *The influence of corrosion pits on the fatigue life of 17-4PH steam turbine blade steel*. Engineering Fracture Mechanics, 2015. **147**: p. 158-175.
83. Jones, R., *Fatigue crack growth and damage tolerance*. Fatigue & Fracture of Engineering Materials & Structures, 2014. **37**(5): p. 463-483.

Highlights

- A novel plasticization induced slow crack-growth model for high-density polyethylene is developed.
- The crack layer theory is modified considering shear yielding in the process zone instead of crazing.
- Plasticization behavior in the pre-saturated state and during the slow crack growth is successfully simulated.
- The newly proposed slow crack growth model shows great accuracy with the experimental results.
- The developed model expands the applicability of the crack layer theory to any plasticizer.